A maternal-effect *Padi6* variant causes nuclear and cytoplasmic abnormalities in oocytes, as well as failure of epigenetic reprogramming and zygotic genome activation in embryos

Carlo Giaccari,[1] Francesco Cecere,[1] Lucia Argenziano,[1] Angela Pagano,[1] Antonio Galvao,[2,3,4,11] Dario Acampora,[5] Gianna Rossi,[6] Bruno Hay Mele,[7] Basilia Acurzio,[1,12] Scott Coonrod,[8] Maria Vittoria Cubellis,[7] Flavia Cerrato,[1] Simon Andrews,[9] Sandra Cecconi,[6] Gavin Kelsey,[2,3,10] and Andrea Riccio[1,5]

[1]Department of Environmental Biological and Pharmaceutical Sciences and Technologies (DiSTABiF), Università degli Studi della Campania "Luigi Vanvitelli," Caserta 81100, Italy; [2]Epigenetics Programme, The Babraham Institute, Cambridge CB22 3AT, United Kingdom; [3]Centre for Trophoblast Research, University of Cambridge, Cambridge CB2 3EG, United Kingdom; [4]Institute of Animal Reproduction and Food Research of the Polish Academy of Sciences, Olsztyn 10-748, Poland; [5]Institute of Genetics and Biophysics (IGB) "Adriano Buzzati-Traverso," Consiglio Nazionale delle Ricerche (CNR), Naples 80131, Italy; [6]Department of Life, Health, and Environmental Sciences, Università dell'Aquila, L'Aquila 67100, Italy; [7]Department of Biology, University of Naples "Federico II," Napoli 80126, Italy; [8]Baker Institute for Animal Health, Cornell University, Ithaca, New York 14853, USA; [9]Bioinformatics Unit, The Babraham Institute, Cambridge CB22 3AT, United Kingdom; [10]Wellcome-MRC Institute of Metabolic Science-Metabolic Research Laboratories, Cambridge CB2 0QQ, United Kingdom

Maternal inactivation of genes encoding components of the subcortical maternal complex (SCMC) and its associated member, PADI6, generally results in early embryo lethality. In humans, SCMC gene variants were found in the healthy mothers of children affected by multilocus imprinting disturbances (MLID). However, how the SCMC controls the DNA methylation required to regulate imprinting remains poorly defined. We generated a mouse line carrying a *Padi6* missense variant that was identified in a family with Beckwith–Wiedemann syndrome and MLID. If homozygous in female mice, this variant resulted in interruption of embryo development at the two-cell stage. Single-cell multiomic analyses demonstrated defective maturation of *Padi6* mutant oocytes and incomplete DNA demethylation, down-regulation of zygotic genome activation (ZGA) genes, up-regulation of maternal decay genes, and developmental delay in two-cell embryos developing from *Padi6* mutant oocytes but little effect on genomic imprinting. Western blotting and immunofluorescence analyses showed reduced levels of UHRF1 in oocytes and abnormal localization of DNMT1 and UHRF1 in both oocytes and zygotes. Treatment with 5-azacytidine reverted DNA hypermethylation but did not rescue the developmental arrest of mutant embryos. Taken together, this study demonstrates that PADI6 controls both nuclear and cytoplasmic oocyte processes that are necessary for preimplantation epigenetic reprogramming and ZGA.

[*Keywords*: DNMT1 localization; imprinting disorders; multilocus imprinting disturbance; *Padi6*; subcortical maternal complex; epigenetic reprogramming; maternal-effect genes; zygotic genome activation]

Supplemental material is available for this article.

Received October 9, 2023; revised version accepted February 15, 2024.

DNA methylation inherited from the gametes is substantially reprogrammed during the oocyte-to-embryo transition (Sendžikaitė and Kelsey 2019). After fertilization, embryonic cells lose oocyte- and sperm-specific DNA methylation and regain totipotency. During preimplantation development, paternally inherited DNA is rapidly demethylated, at least in part involving activity of ten-eleven translocation (TET) enzymes, whereas maternally inherited DNA methylation is lost in a passive

Present addresses: [11]Department of Comparative Biomedical Sciences, Royal Veterinary College, London NW1 0TU, UK; [12]Epigenetics and Neurobiology Unit, European Molecular Biology Laboratory (EMBL), 00015 Monterotondo, Italy.
Corresponding authors: andrea.riccio@unicampania.it, gavin.kelsey@babraham.ac.uk

Article published online ahead of print. Article and publication date are online at http://www.genesdev.org/cgi/doi/10.1101/gad.351238.123. Freely available online through the *Genes & Development* Open Access option.

manner during cellular proliferation through nuclear exclusion of DNMT1 and its accessory protein, UHRF1 (Chen and Zhang 2020). Set against this global trend, imprinted genes need to retain their gamete of origin DNA methylation (Barlow and Bartolomei 2014). Immediately after fertilization, the zygotic genome is transcriptionally silent and early embryo development is controlled by maternal mRNAs and proteins (Aoki 2022). Zygotic genome activation (ZGA) in mice is initiated between the mid-one-cell and early two-cell stages (minor ZGA) and proceeds during the mid to late two-cell stage (major ZGA) (Aoki 2022).

In mammals, the subcortical maternal complex (SCMC) is a multiprotein complex that has been associated with multiple biological functions occurring during the oocyte-to-embryo transition (Li et al. 2008; Bebbere et al. 2021). A number of proteins have been demonstrated or proposed to be part of the SCMC, including KHDC3L, OOEP, PADI6, TLE6, and ZBED3, as well as several NLRP family members (NLRP2, NLRP4f, NLRP5, NLRP9a/b/c, and, in humans, NLRP7) (Bebbere et al. 2021). All SCMC proteins are encoded by maternal-effect genes. PADI6 is an oocyte-specific protein belonging to the peptidylarginine deiminase (PAD) protein family but without evident enzymatic activity in vitro (Raijmakers et al. 2007; Williams and Walport 2023). Maternal PADI6 is required for embryo development beyond the two-cell stage and formation of the oocyte lattices that are cytoplasmic structures believed to work as ribosomal storage for the early embryo (Esposito et al. 2007). A recent study demonstrated that these cytoplasmic lattices contain PADI6 and other SCMC proteins and are associated with many proteins that are protected from degradation and later used during early embryo development (Jentoft et al. 2023). Furthermore, maternal *Padi6* mutant two-cell embryos have ribosomal components and de novo protein synthesis that are impaired, as well as drastically reduced transcription levels (Yurttas et al. 2008).

In humans, biallelic loss-of-function mutations of *PADI6* are associated with female infertility and hydatidiform moles (Qian et al. 2018). Furthermore, both biallelic and monoallelic *PADI6* variants have been found in the healthy mothers of children affected by genomic imprinting disorders (Eggermann et al. 2022; Williams and Walport 2023).

Genomic imprinting is the gamete of origin-dependent epigenetic marking and expression of genes and is required for normal development (Barlow and Bartolomei 2014). In humans, its deregulation affects growth, metabolism, and neurological functions (Eggermann et al. 2023). Imprinting disorders are associated with single- or multilocus DNA methylation abnormalities, which in turn can be traced back to genetic variants occurring in *cis* or in *trans* (Monk et al. 2019). In particular, maternal-effect SCMC gene variants are associated with multilocus imprinting disturbance (MLID) (see Eggermann et al. 2022). Very little is known about the mechanisms linking the SCMC and DNA methylation. So far, it has been demonstrated that a hypomorphic *KHDC3L* variant results in globally impaired de novo methylation in human oocytes (Demond et al. 2019), whereas *Nlrp2* knockout in mice leads to abnormal subcellular localization of DNMT1 in oocytes and DNA methylation abnormalities in mouse embryos (Mahadevan et al. 2017; Yan et al. 2023) and impacts expression of the histone demethylase KDM1B (Anvar et al. 2023). More recently, it has been shown that the maternal knockout of a further but not SCMC-associated *Nlrp* gene (*Nlrp14*) also results in altered localization of DNMT1 and genomic hypermethylation in early embryos (Yan et al. 2023).

Since inactivation of SCMC genes generally leads to early embryo lethality, studying the mechanisms by which these maternal-effect genes control maternal-to-zygotic transition in mammals has been challenging. Here, we describe a mouse line carrying a variant of the *PADI6* gene found in the genome of the mother of two siblings affected by Beckwith–Wiedemann syndrome (BWS) and MLID (Cubellis et al. 2020). By applying a method of combined single-cell profiling of gene expression and DNA methylation, we investigated the molecular changes occurring in early development. We found that, if present in the mother, this variant severely affected early mouse development. Through nuclear and cytoplasmic abnormalities, *Padi6* mutant oocytes lead to impairments in epigenetic reprogramming and ZGA.

Results

Generation of the Padi6^{P620A} *mouse line*

To study the role of maternal-effect *Padi6* variants in DNA methylation programming and imprinting, we generated a knock-in mouse line modeling the human missense mutation P632A that was found in compound heterozygosity with a truncating mutation in a family with two siblings affected by Beckwith–Wiedemann syndrome and MLID (Cubellis et al. 2020). Proline 632 is located in a highly conserved region of the PADI6 protein and corresponds to residue 620 of the mouse protein (Supplemental Fig. S1A). So, the variant chromosome 4, g.140727767 C→G; P620A of *Padi6* exon 16 was introduced into the genome of mouse embryonic stem cells (ESCs) by homologous recombination through the use of a FLP/frt system vector (Supplemental Fig. S1B). The presence of the mutation in ESC clones was demonstrated by Sanger sequencing and Southern blotting analysis (Supplemental Fig. S1C,D). Chimeric mice were then obtained by injection of the positive clones into mouse blastocysts, and germline transmission was confirmed by PCR. To remove the Neo cassette, the knock-in mouse line was crossed with a line carrying the *Flp* recombinase gene, and excision was confirmed by PCR (Supplemental Fig. S1E). To exclude any possible rearrangement during recombination, we determined the whole-genome sequence of somatic DNA of a *Padi6*$^{P620A/P620A}$ female mouse. We confirmed the presence of the chromosome 4, g.140727767 C→G variant and demonstrated the absence of any CNV or structural variant involving the *Padi6* gene (Supplemental Fig. S1F; data not shown).

Phenotypic characterization of the Padi6^{P620A} *mouse line*

From heterozygous *Padi6*$^{P620A/+}$ interbreeding, we obtained 12 litters, including 23 *Padi6*$^{+/+}$, 40 *Padi6*$^{P620A/+}$, and 26 *Padi6*$^{P620A/P620A}$ pups, a ratio that did not significantly differ from the expected genotype distribution ($X^2 = 0.6192$, $P = 0.4313$) (Fig. 1A). Both *Padi6*$^{P620A/+}$ and *Padi6*$^{P620A/P620A}$ mice were viable, did not display any visible morphological anomaly, and grew normally with normal life spans. Similar to *Padi6*$^{+/+}$ animals, all follicular stages and corpora lutea were observed in the ovaries of 4- to 8-wk-old *Padi6*$^{P620A/+}$ and *Padi6*$^{P620A/P620A}$ females (Fig. 1B,C; data not shown). Similar levels of *Padi6* mRNA were demonstrated in MII oocytes of the *Padi6*$^{+/+}$ and *Padi6*$^{P620A/P620A}$ mice by single-cell RNA sequencing (scRNA-seq) analysis (Fig. 1D). However, while the PADI6 protein was strongly detected in the ovary and correctly localized in the oocyte cytoplasm of the control mice (Kim et al. 2010), we found that its level was decreased in the *Padi6*$^{P620A/P620A}$ mice, below the detection levels of Western blotting and immunofluorescence (Fig. 1E–G). Next, we tested whether the *Padi6* P620A variant affected mouse fertility. We obtained litters of similar size from natural matings between 2- to 4-mo-old *Padi6*$^{+/+}$ and *Padi6*$^{P620A/+}$ females and *Padi6*$^{+/+}$ males. In contrast, *Padi6*$^{P620A/P620A}$ females were completely unable to have pups (Fig. 1H). We performed a similar study on male fertility, but no significant difference was observed in litter size from 2- to 4-mo-old *Padi6*$^{+/+}$, *Padi6*$^{P620A/+}$, or *Padi6*$^{P620A/P620A}$ males crossed with *Padi6*$^{+/+}$ females (Fig. 1I). Thus, the P620A variant causes a strong reduction of the PADI6 protein level and profoundly affects female fertility but has no effect on male fertility.

In silico studies show that the P620A variant destabilizes the PADI6 structure

The finding that the *Padi6*$^{P620A/P620A}$ oocytes correctly transcribed the *Padi6* gene but failed to accumulate the PADI6 protein was unexpected because the human P632A variant was predicted to be stabilizing by the prediction tool site-directed mutator (SDM) but deleterious by sorting intolerant from tolerant (SIFT) and possibly damaging by polymorphism phenotyping v2 (Polyphen-v2) (Cubellis et al. 2020). We reanalyzed the impact of the orthologous human and mouse variants on the PADI6 protein by using the more recent and integrated computational method DynaMut, assessing changes in protein stability and flexibility (Rodrigues et al. 2018), and two further structure-based prediction tools, mutation cutoff scanning matrix (mCSM) and DUET (combining mCSM and SDM) (Pires et al. 2014a,b). Using these tools, both variants were predicted to be destabilizing, with a more severe effect in mice (ΔΔG, −0.715 vs. −0.246) (Supplemental Table S1). To better understand this difference, we analyzed the structural models of human and mouse PADI6 (https://alphafold.ebi.ac.uk/entry/Q6TGC4 and https://alphafold.ebi.ac.uk/entry/Q8K3V4, for the human and mouse proteins, respectively). We observed that P632 in humans and P620 in mice are in the middle of a stretch of eight identical amino acids forming a polyproline II helix and an isolated β-strand (Supplemental Tables S2, S3) that have a high propensity for protein–protein interaction (Cubellis et al. 2005). Both human P632A and mouse P620A variants increase the flexibility of the protein in this area according to DynaMut (Supplemental Fig. S2A); thus, an effect on the relative positions of side chains can be envisaged. We then analyzed the amino acids that are in spatial proximity (5 Å) of the mutations (Supplemental Fig. S2B). We found a single nonconservative variation between humans and mice. In humans, there is a triad formed by Pro632, Leu617, and Phe660, which in mice correspond to Pro620, Met605, and Phe648; thus, a methionine–aromatic motif, which plays a special role in protein stabilization (Valley et al. 2012), is present only in the mouse protein. We predicted with DynaMut the effect of Met605Ala or Phe648Ala variants on protein stability and found that they were both destabilizing to an extent that is even higher than that of Pro620Ala (Supplemental Table S1). In conclusion, in silico predictions suggest that the increased flexibility due to the P620A variant may disturb the stabilizing Met605–Phe648 interaction in the mouse PADI6 protein.

The Padi6$^{P620A/P620A}$ *oocytes show normal expression of SCMC components but altered subcellular localization of OOEP*

To study the effect of the *Padi6*^{P620A} variant on the SCMC, we determined the expression of the other components of the complex in oocytes. RT-qPCR and scRNA-seq analyses revealed no significant difference in the expression of the *Ooep*, *Nlrp5*, and *Tle6* genes among *Padi6*$^{+/+}$, *Padi6*$^{P620A/+}$, and *Padi6*$^{P620A/P620A}$ ovaries and *Padi6*$^{+/+}$ and *Padi6*$^{P620A/P620A}$ germinal vesicle (GV) oocytes (Fig. 2A,B). Similarly, comparable NLRP5 and TLE6 protein levels were detected in *Padi6*$^{+/+}$, *Padi6*$^{P620A/+}$, and *Padi6*$^{P620A/P620A}$ ovaries by Western blot analysis (Fig. 2C). However, different results were obtained by immunofluorescence. While typical subcortical localization of OOEP was observed in the GV oocytes of *Padi6*$^{+/+}$ mice, reduced cytoplasmic fluorescence and increased signal in the nucleus were found in the *Padi6*$^{P620A/P620A}$ mutants (Fig. 2D). Differently from OOEP, the subcellular localization of NLRP5 and TLE6 was not changed in the mutant GV oocytes (Fig. 2E,F). These results indicate that the *Padi6*^{P620A} variant does not affect the expression of several SCMC components but modifies the subcellular localization of OOEP.

Developmental failure and abnormal cell divisions of Padi6$^{MatP620A/+}$ *embryos*

To investigate whether the infertility of *Padi6*$^{P620A/P620A}$ female mice was caused by embryonic death, we performed in vitro fertilization (IVF) experiments with ovulated MII oocytes collected from *Padi6*$^{+/+}$ and *Padi6*$^{P620A/P620A}$ females. After hormonal treatment, no difference in the number of ovulated eggs was observed between

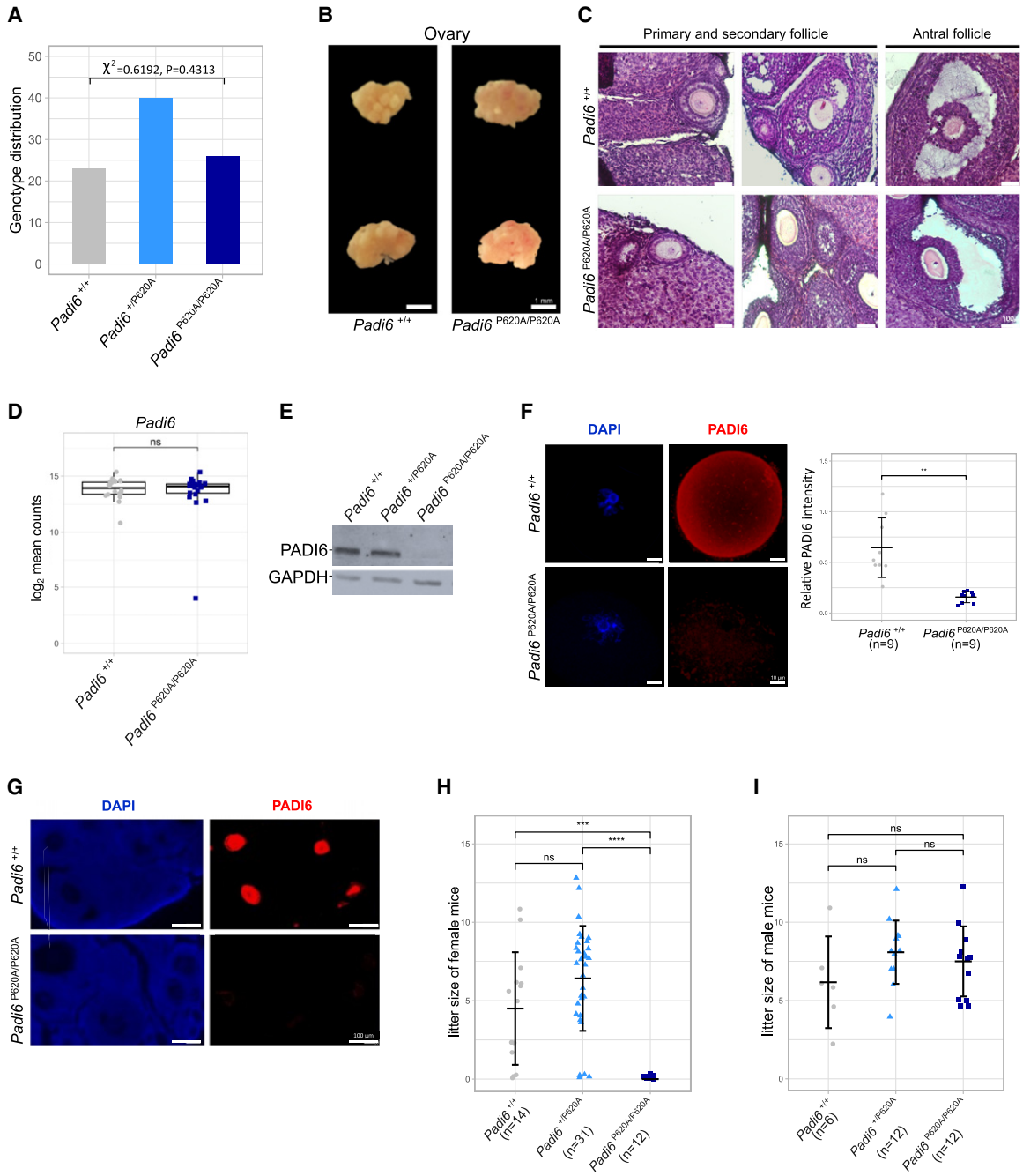

Figure 1. Characterization of the mouse line carrying the *Padi6*^{P620A} mutation. (*A*) Genotype distribution of the offspring derived from *Padi6*$^{P620A/+}$ matings. (*B*) Comparison of morphological characteristics between *Padi6*$^{+/+}$ and *Padi6*$^{P620A/P620A}$ ovaries. The mice were derived from the same litter, and the ovaries were collected from 8-wk-old females. (*C*) Hematoxylin and eosin staining on paraffin-embedded *Padi6*$^{+/+}$ (*top*) and *Padi6*$^{P620A/P620A}$ (*bottom*) ovaries; the *left* and *middle* panels show primary and secondary follicles, and the *right* panel shows an antral follicle. (*D*) Box plot representing the *Padi6* expression level calculated from $\log_2$ mean counts of scRNA-seq data of 18 *Padi6*$^{+/+}$ (gray) and 20 *Padi6*$^{P620A/P620A}$ (blue) MII oocytes. (*E*) Western blotting analysis of PADI6 and GAPDH in *Padi6*$^{+/+}$, *Padi6*$^{+/P620A}$, and *Padi6*$^{P620A/P620A}$ ovaries. The data shown are representative of three independent experiments. (*F*, *left*) Representative images of immunostaining of *Padi6*$^{+/+}$ (*top*) and *Padi6*$^{P620A/P620A}$ (*bottom*) GV oocytes with anti-PADI6 antibodies (red) and DAPI (blue). (*Right*) Quantification of PADI6 immunostaining intensity. "*n*" denotes the number of oocytes analyzed in three independent experiments. (*G*) Representative images of paraffin-embedded ovarian sections from 8-wk-old *Padi6*$^{+/+}$ (*top*) and *Padi6*$^{P620A/P620A}$ (*bottom*) mice immunostained with anti-PADI6 antibodies (red) and DAPI (blue). Consistent results were obtained in two independent experiments. (*H*,*I*) Female (*H*) and male (*I*) fertility of *Padi6*$^{+/+}$ (gray), *Padi6*$^{P620A/+}$ (light blue), and *Padi6*$^{P620A/P620A}$ (blue) mice; 2- to 4-mo-old females (*H*) and males (*I*) of the indicated genotypes were mated with *Padi6*$^{+/+}$ males and females, respectively. "*n*" denotes the number of mice analyzed. The data shown in *D*, *F*, *H*, and *I* are mean ± SD and were analyzed using an unpaired two-tailed Student's *t*-test. (ns) $P > 0.05$, (**) $P < 0.01$, (***) $P < 0.001$, (****) $P < 0.0001$.

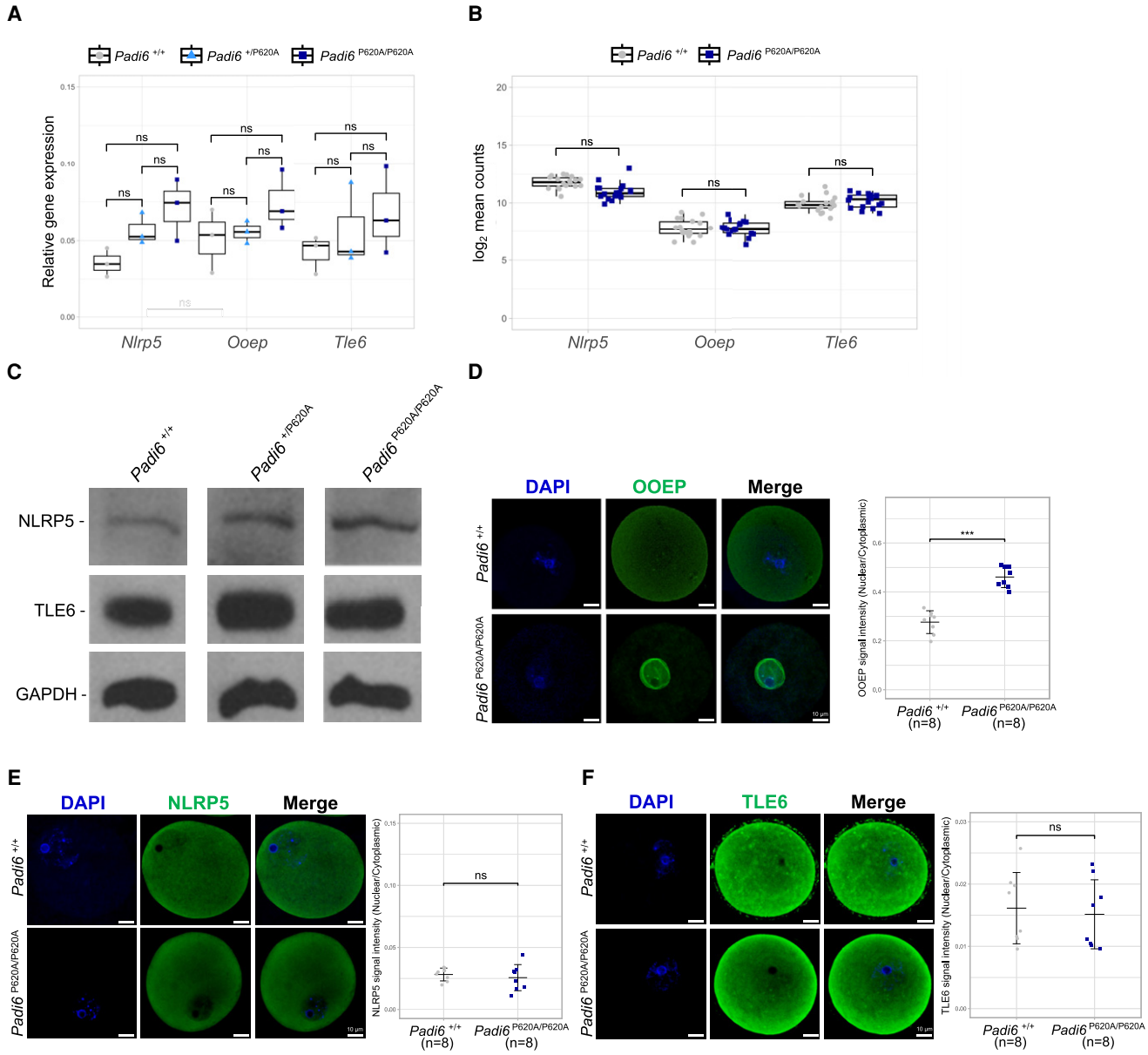

Figure 2. Effect of the *Padi6*^{P620A} variant on gene expression and protein level of the components of the SCMC. (*A*) Box plot showing *Nlrp5*, *Ooep*, and *Tle6* gene expression analysis in *Padi6*$^{+/+}$ (gray), *Padi6*$^{P620A/+}$(light blue), and *Padi6*$^{P620A/P620A}$ (blue) ovaries, as assessed by RT-qPCR, after normalization against the level of β-*actin*. Each dot represents a single replicate of three independent experiments. (*B*) Box plot showing the *Nlrp5*, *Ooep*, and *Tle6* expression levels calculated with $\log_2$ mean counts of scRNA-seq data of 18 *Padi6*$^{+/+}$ (gray) and 20 *Padi6*$^{P620A/P620A}$ (blue) MII oocytes. Each dot represents a single MII oocyte. (*C*) Western blot analysis of NLRP5, TLE6, and GAPDH in *Padi6*$^{+/+}$, *Padi6*$^{+/P620A}$, and *Padi6*$^{P620A/P620A}$ ovaries. The data shown are representative of three independent experiments. (*D*, *left*) Representative images of immunostaining of *Padi6*$^{+/+}$ (*top*) and *Padi6*$^{P620A/P620A}$ (*bottom*) GV oocytes with anti-OOEP antibodies (green) and DAPI (blue). (*Right*) Quantification of the OOEP nuclear/cytoplasmic ratio. (*E*, *left*) Representative images of immunostaining of *Padi6*$^{+/+}$ (*top*) and *Padi6*$^{P620A/P620A}$ (*bottom*) GV oocytes with anti-NLRP5 antibodies (green) and DAPI (blue). (*Right*) Quantification of the NLRP5 nuclear/cytoplasmic ratio. (*F*, *left*) Representative images of immunostaining of *Padi6*$^{+/+}$ (*top*) and *Padi6*$^{P620A/P620A}$ (*bottom*) GV oocytes with anti-TLE6 antibodies (green) and DAPI (blue). (*Right*) Quantification of the TLE6 nuclear/cytoplasmic ratio. In *D*–*F*, "*n*" denotes the number of oocytes analyzed in three independent experiments. The data shown in *A*, *B*, and *D*–*F* are mean ± SD and were analyzed using an unpaired two-tailed Student's *t*-test. (ns) $P > 0.05$, (***) $P < 0.001$.

Padi6$^{P620A/P620A}$ and *Padi6*$^{+/+}$ females (Fig. 3A). Also, both genotypes of mice showed a success rate of fertilization >50% (65% and 55% of two-cell embryos for *Padi6*$^{+/+}$ and *Padi6*$^{P620A/P620A}$ oocytes, respectively) 24 h after the start of IVF (Fig. 3B). Greater differences between the two groups began to appear 48 h following IVF (Fig. 3C,D). While all the *Padi6*$^{+/+}$ two-cell embryos continued to develop normally, only 24% of the embryos derived from

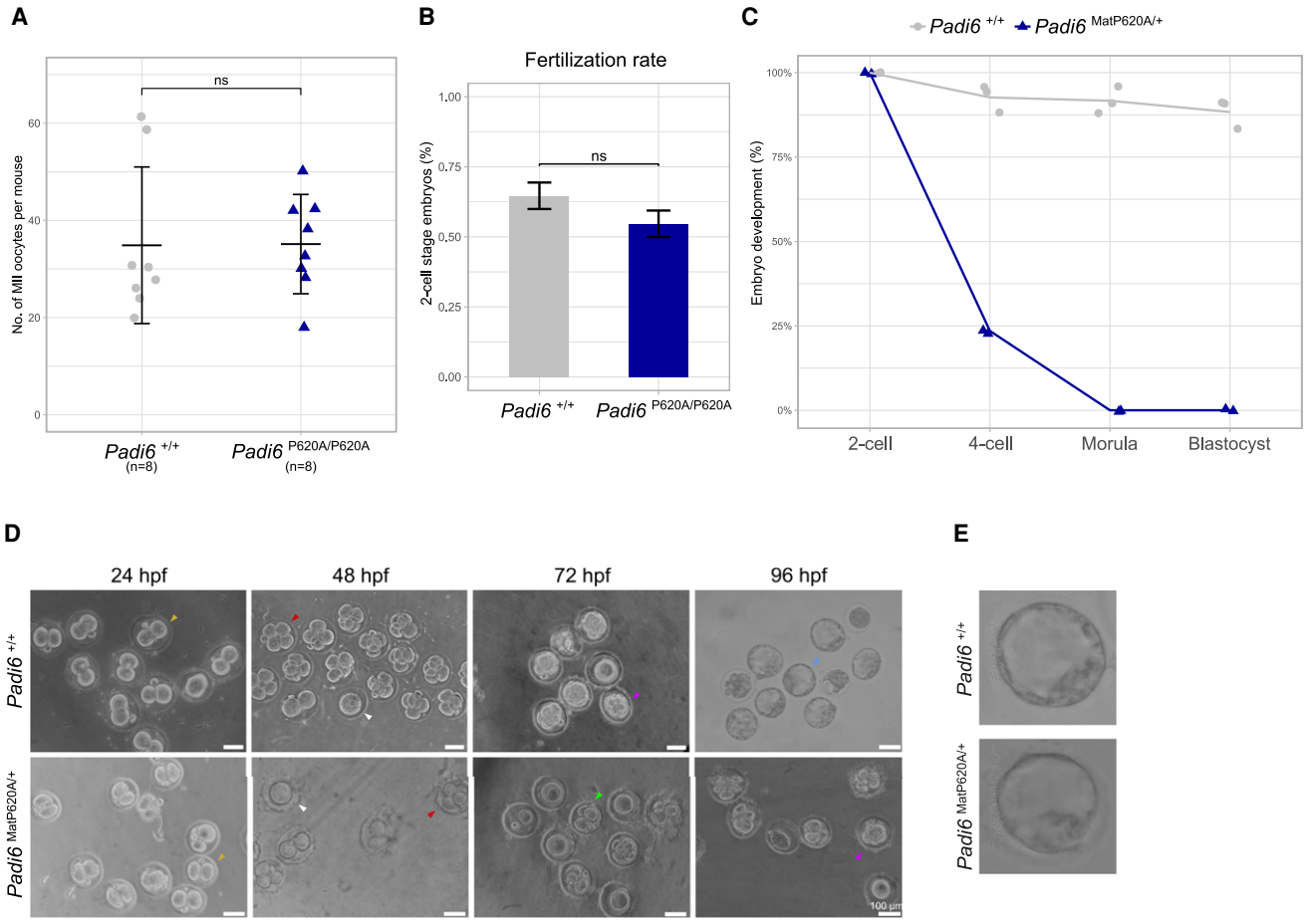

Figure 3. Effect of *Padi6*^{P620A} variant on IVF and embryo development. (*A*) Number of MII oocytes ovulated per female mouse after PMSG + hCG hormone treatment. "*n*" denotes the number of females analyzed. (*B*) Bar plot representing the fertilization rate after IVF of MII oocytes from 8-wk-old *Padi6*$^{+/+}$ (gray) and *Padi6*$^{P620A/P620A}$ (blue) females with wild-type sperm. (*C*) Line plot showing the percentage of *Padi6*$^{+/+}$ (gray) and *Padi6*$^{MatP620A/+}$ (blue) embryos developed after IVF. Each dot and triangle represents an independent experiment. (*D*) Representative still frames of *Padi6*$^{+/+}$ (*top*) and *Padi6*$^{MatP620A/+}$ (*bottom*) embryos at 24, 48, 72, and 96 h after IVF. Arrowheads indicate different developmental stages: unfertilized oocyte (white), two-cell embryo (yellow), four-cell embryo (red), morula (purple), blastocyst (light blue), and abnormal embryo (light green). (*E*) Representative examples of *Padi6*$^{+/+}$ (*top*) and *Padi6*$^{MatP620A/+}$ (*bottom*) blastocysts. The data shown in *A* and *B* are mean ± SD and were analyzed using an unpaired two-tailed Student's *t*-test. (ns) $P > ^{***}$ 0.05,

Padi6$^{P620A/P620A}$ females (referred to here as *Padi6*$^{MatP620A/+}$ embryos) were able to reach the four-cell stage. After 72 h, most of the control embryos had reached the morula stage (95%). In contrast, the *Padi6*$^{MatP620A/+}$ embryos showed significant impairment of embryonic development, with the majority blocked at the two- or four-cell stages and a small percentage blocked at the eight-cell stage, and many displayed a reduced number of blastomers and/or morphologic abnormalities and/or asymmetric cell divisions (Fig. 3C,D). Thus, after 3 d of development, almost all the *Padi6*$^{MatP620A/+}$ embryos were either degenerated or arrested. After 96 h, control embryos reached the blastocyst stage, while only a small percentage of *Padi6*$^{MatP620A/+}$ embryos showed a degree of compaction similar to morula (Fig. 3D). More than 120 h after IVF, very few *Padi6*$^{MatP620A/+}$ embryos with a blastocyst-like morphology were found (Fig. 3E). In summary, the *Padi6*^{P620A} variant displayed a maternal-effect phenotype with abnormal embryonic development and was mostly interrupted at the two-cell stage, if present in homozygosity.

The Padi6^{P620A} *variant leads to transcriptome differences indicative of defective oocyte maturation*

To look for the effect of the *Padi6*^{P620A} variant on the oocyte transcriptome, we analyzed MII oocytes by scRNA-seq. Comparison of the scRNA-seq data sets of the *Padi6*$^{+/+}$ and *Padi6*$^{P620A/P620A}$ oocytes by global principal component analysis (PCA) resulted in some degree of separation along principal component 1 (PC1), particularly for the *Padi6*$^{P620A/P620A}$ cells (Fig. 4A). We detected 706 genes as being differentially expressed ($|\log_2 FC| \geq 1$, FDR < 0.01) and defined them as MII-DEGs (Supplemental Table S4). Out of these, 117 were down-regulated and 589 were up-regulated (Fig. 4B; Supplemental Fig. S3A). Using

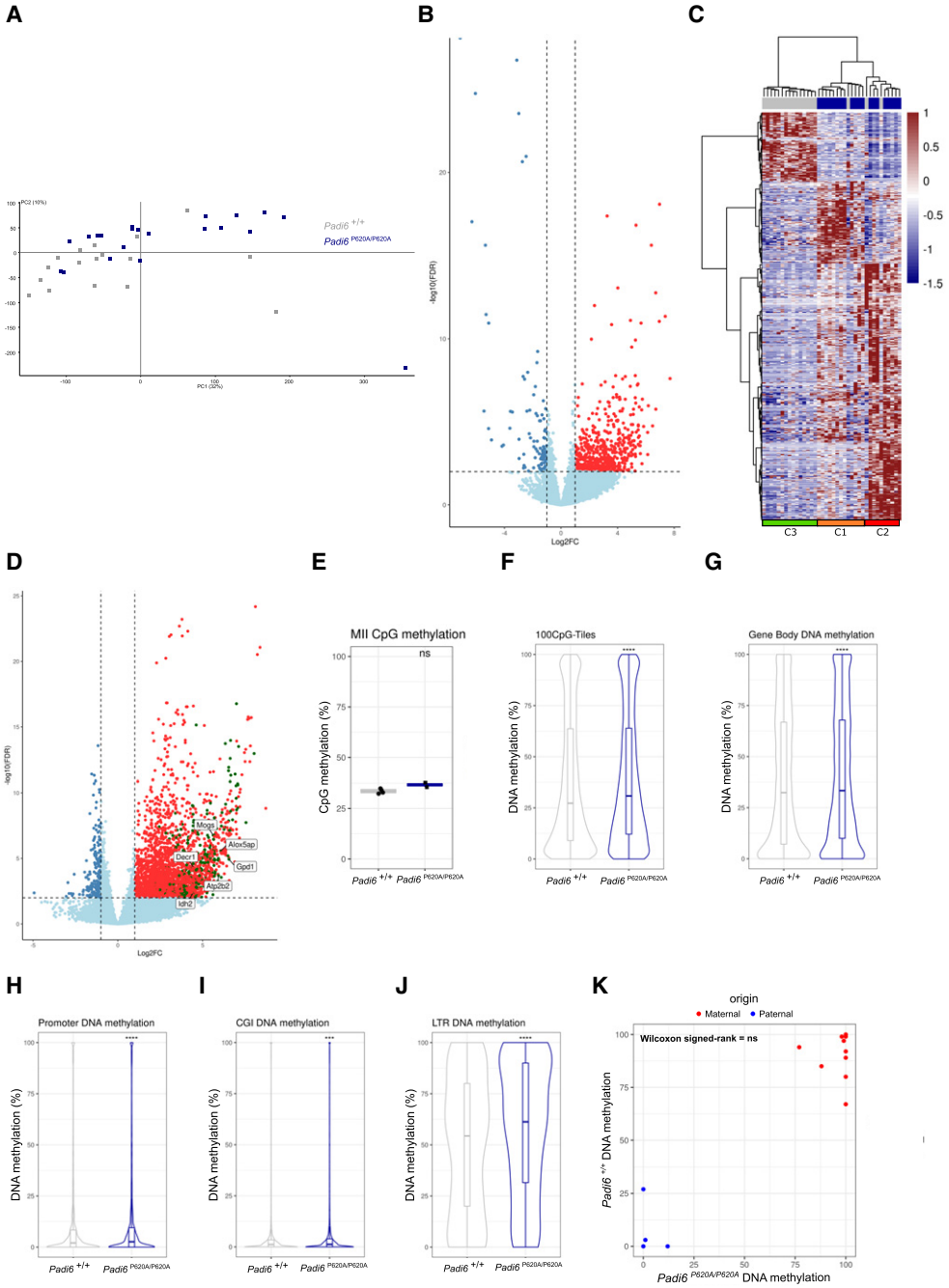

Figure 4. scRNA-seq and scBS-seq analyses of *Padi6*$^{P620A/P620A}$ and *Padi6*$^{+/+}$ MII oocytes. (*A*) PCA of all the genes covered by the scRNA-seq experiment. Principal component 1 (PC1) is plotted on the *x*-axis and principal component 2 (PC2) is displayed on the *y*-axis. Each dot corresponds to an MII oocyte, and gray and blue indicate the Padi6$^{+/+}$ and Padi6$^{P620A/P620A}$ genotypes, respectively. (*B*) Volcano plot displaying the differentially expressed genes (DEGs) between Padi6$^{P620A/P620A}$ and Padi6$^{+/+}$ MII oocytes. The $\log_2$ fold change ($\log_2$FC) is reported on the *x*-axis, and the significance expressed as $-\log_{10}$(FDR). The dashed lines represent the thresholds used for DEGs ($|\log_2 FC| > 1$ and FDR < 0.01) on the *y*-axis. The up-regulated genes are displayed in red, and the down-regulated genes are shown in blue. (*C*) Heat map displaying the DEGs between the *Padi6*$^{P620A/P620A}$ and *Padi6*$^{+/+}$ MII oocytes. Columns represent different samples, and rows represent different genes. Hierarchical clustering identifies three clusters: cluster 1 (orange), cluster 2 (red), and cluster 3 (green). The expression profile is represented as scaled FPKM. (*D*) Volcano plots displaying the DEGs between cluster 2 and cluster 3 (C2-DEGs). The up-regulated and the down-regulated genes are reported as red and blue dots, respectively. The green dots represent GV markers. $\log_2$ fold change ($\log_2$FC) is reported on the *x*-axis, and significance is expressed as $-\log_{10}$(FDR) on the *y*-axis. (*E*) Box plot displaying the percentage CpG methylation of each MII oocyte as assessed by scBS-seq and passing quality control. (*F–J*) Violin and box plots displaying the DNA methylation level of the whole genome divided into 100-CpG tiles (*F*), gene bodies (*G*), promoter regions (TSS-3000+100) (*H*), CpG islands (*I*), and LTR elements (*J*) of the *Padi6*$^{P620A/P620A}$ and *Padi6*$^{+/+}$ MII oocytes. In each case, the violin plots represent the merged data from two *Padi6*$^{P620A/P620A}$ and four *Padi6*$^{+/+}$ MII oocytes. (*K*) Dot plot displaying the DNA methylation level of the imprinted germline DMRs in *Padi6*$^{P620A/P620A}$ (*x*-axis) and *Padi6*$^{+/+}$ (*y*-axis) MII oocytes. Red and blue dots represent the DMRs that are methylated in oocytes and sperm, respectively. The data shown in *E–K* were analyzed using Wilcoxon signed ranked test. (ns) $P > 0.05$, (***) $P < 0.001$, (****) $P < 0.0001$.

the MII-DEGs, three different clusters of oocytes were identified by unsupervised hierarchical clustering of scRNA-seq data (Fig. 4C). Clusters 1 and 2 corresponded to most of the *Padi6*$^{P620A/P620A}$ oocytes, and cluster 3 corresponded to most of the *Padi6*$^{+/+}$ oocytes, thus demonstrating two groups of mutant oocytes according to their RNA profiles. In particular, a subset of DEGs ($n = 345$) was up-regulated in cluster 2 but showed heterogeneous expression in cluster 1 (Fig. 4C; Supplemental Table S5). To better investigate the genes that were characteristic of clusters 1 and 2, we compared the expression profiles of clusters 1 and 2 with those of cluster 3. When compared with cluster 3, we found 2729 DEGs (C2-DEGs; FDR < 0,01, $|\log_2 FC| > 1$) that were differentially expressed in cluster 2 and not in cluster 1, and 108 DEGs (C1-DEGs; FDR < 0,01, $|\log_2 FC| > 1$) that were specific to cluster 1 (Supplemental Table S6). Gene ontology analysis of the C2-DEGs revealed an enrichment of genes related to metabolic processes (GO:BP) and to cellular anatomical structure, organelles, and cytoplasm (GO:CC) (Supplemental Fig. S3B). Interestingly, we found that 313 up-regulated genes were reported as GV oocyte markers (Fig. 4D; Supplemental Fig. S3C; Supplemental Table S7; Zhao et al. 2020). For instance, the genes *Idh2*, *Mogs*, *Gpd1*, *Decr1*, *Alox5ap*, and *Atp2b2*, which stimulate energy production, glycosylation, lipid metabolism, and calcium signaling, were up-regulated (Fig. 4D; Supplemental Fig. S3D). Overall, these results indicate that the *Padi6*$^{P620A/P620A}$ variant affects the correct maturation of MII oocytes.

Whole-genome methylation profiles of the MII oocytes were determined by using single-cell bisulfite sequencing (scBS-seq). We found limited changes in the distribution of DNA methylation in the whole genome, gene bodies, promoters, CpG islands (CGIs), promoters, and LTRs (Fig. 4E–J; Supplemental Tables S8–S12) but no significant difference in low-complexity regions, LINEs, and simple repeats (Supplemental Fig. S3E) between the *Padi6*$^{P620A/P620A}$ and *Padi6*$^{+/+}$ oocytes. No significant difference in the methylation of the imprinted germline DMRs was found as well (Fig. 4K; Supplemental Fig. S3F). Due to limited coverage and the low number of samples analyzed in the BS-seq, we were not able to correlate the DNA methylation differences with the gene expression changes or exclude subtle differences in the genomic DNA methylation pattern. In summary, *Padi6*$^{P620A/P620A}$ MII oocytes demonstrated altered RNA profiles with respect to controls, which in part corresponded to an elevated abundance of transcripts typical of immature oocyte stages and deregulation of transcripts involved in cytoplasmic functions. Whole-genome DNA methylation was only slightly affected, and methylation imprinting was unchanged.

Padi6$^{MatP620A/+}$ *embryos show failure of ZGA and epigenetic reprogramming*

To better investigate the molecular basis of the developmental arrest of the embryos derived from *Padi6*$^{P620A/P620A}$ oocytes, we determined the transcriptome of the two-cell embryos generated by IVF. This analysis revealed 624 2c-DEGs (FDR < 0.05) between the *Padi6*$^{MatP620A/+}$ and *Padi6*$^{+/+}$ embryos. Among these, 395 were down-regulated and 229 were up-regulated (Fig. 5A; Supplemental Table S13). To investigate the possible role of the 2c-DEGs during maternal-to-zygotic transition, we first identified the genes that were differentially expressed between the *Padi6*$^{+/+}$ MII oocytes and two-cell embryos. This analysis revealed 2146 up-regulated and 2643 down-regulated genes that we defined as ZGA and maternal-decay (Mat-decay) genes, respectively (Supplemental Table S14). Using these genes as a reference, we found that 265 ZGA and 113 Mat-decay genes were deregulated in the *Padi6*$^{MatP620A/+}$ two-cell embryos. Interestingly, 95% of these ZGA 2c-DEGs were down-regulated and 93% of the Mat-decay 2c-DEGs were up-regulated (Fig. 5B; Supplemental Table S15). Notably, 25% of these deregulated ZGA genes were related to major ZGA, 4% were related to minor ZGA, and 22% were classified as minor and major ZGA genes (Fig. 5B; Wang et al. 2022). In particular, we found normal expression levels of the *Dux* family genes, known to be involved in minor ZGA, and down-regulation of genes strongly associated with major ZGA, such as the *Zscan* family, the *Tcstv* family, and *Zfp352* (Fig. 5C). To investigate the impact of the 2c-DEGs on embryo development, we performed a STRING *k*-mean cluster analysis and found that 71 out of the 378 deregulated gene products interacted and could be sorted into four clusters associated with different functions ([1] histone binding, [2] RNA binding, [3] regulation of RNA polymerase activity, and [4] heterogeneous pathways, including leukemia inhibitory factor receptor and inositol triphosphate kinase pathways), indicating a cross-talk between the affected ZGA and Mat-decay genes, which may underlie the two-cell development arrest of the *Padi6*$^{MatP620A/+}$ embryos (Supplemental Fig. S4A,B). To understand the cell cycle dynamics and potential regulatory differences between the two genotypes, we inferred the cell cycle phase across cells by analyzing the genes that are expressed in a cell cycle-regulated manner. We found that the percentage of cells in the G1 phase was equal for both genotypes, but there was a noticeable difference in the S and G2/M phases (Fig. 5D; Supplemental Table S16). While the wild-type blastomeres were mostly in G2/M, half of the mutant ones were in S phase, and only five out of 18 were in G2/M. These results suggest a delay or an extended duration of the S phase in the *Padi6*$^{MatP620A/+}$ embryos and a quicker transition through the S phase to G2/M in the *Padi6*$^{+/+}$ embryos.

As in the MII oocytes, we tested whole-genome methylation by scBS-seq. The results obtained demonstrated a global hypermethylation of *Padi6*$^{MatP620A/+}$ embryos compared with *Padi6*$^{+/+}$ embryos (Fig. 5E,F; Supplemental Table S17). This increase involved promoter regions, LINEs, LTRs, and simple repeats (Fig. 5G–I; Supplemental Fig. S5A; Supplemental Tables S18, S19). In particular, by sorting the LINEs on the basis of their evolutionary age (Sookdeo et al. 2013), we found that the younger elements were more strongly hypermethylated than the older ones (Fig. 5H; Supplemental Fig. S5B; Supplemental Table S20). Moreover, we found highly significant hypermethylation in subfamilies of endogenous retroviruses, including

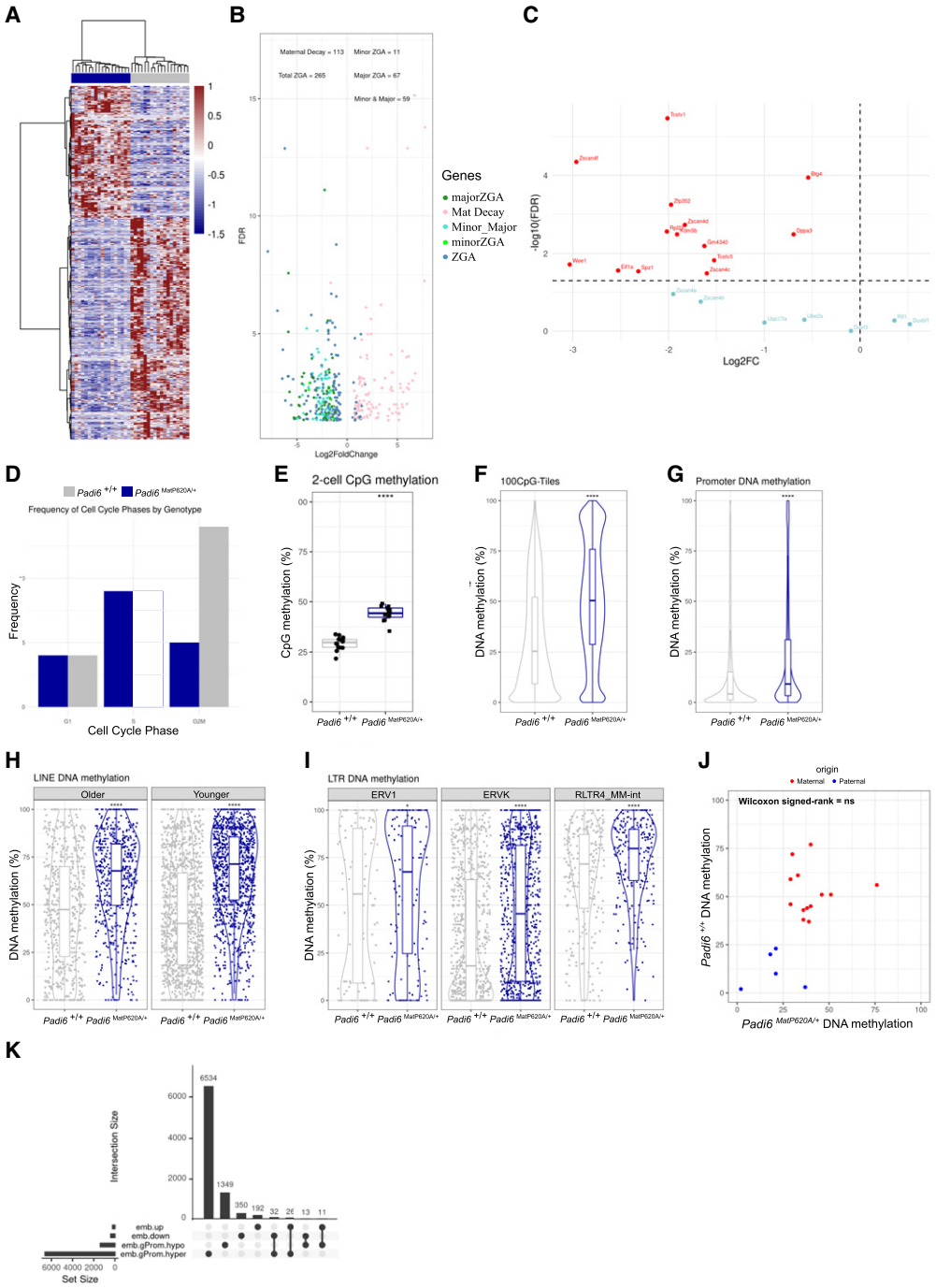

Figure 5. scRNA-seq and BS-seq analyses of *Padi6*$^{MatP620A/+}$ two-cell embryos. (*A*) Heat map displaying the 624 DEGs between the *Padi6*$^{P620A/+}$ and *Padi6*$^{+/+}$ two-cell embryos. Note that two distinct clusters characterized by the two different genotypes segregate by hierarchical clustering. The expression profile is represented as scaled FPKM. (*B*) Volcano plot displaying color-coded DEGs based on their role in ZGA or maternal decay. (*C*) Dot plot showing the differential expression of genes with important roles in ZGA. The $\log_2$ fold change ($\log_2$FC) is reported on the *x*-axis, and the significance expressed as $-\log_{10}$(FDR) is displayed on the *y*-axis. (*D*) Bar plot showing the distribution of the cell cycle phases (G1, S, and G2/M) in *Padi6*$^{MatP620A/+}$ (blue) and *Padi6*$^{+/+}$ (gray) two-cell blastomeres. (*E*) Box plot displaying the CpG methylation in the two-cell embryo cells. (*F–I*) Violin and box plots displaying the DNA methylation of the whole genome divided into 100-CpG tiles (*F*), promoter regions (TSS-3000+100) (*G*), old and younger LINEs (*H*), and LTR subclasses (*I*) of the *Padi6*$^{MatP620A/+}$ and *Padi6*$^{+/+}$ two-cell embryos. In each case, the violin plots represent the merged data from 12 *Padi6*$^{MatP620A/+}$ and 14 *Padi6*$^{+/+}$ two-cell embryo cells. (*J*) Dot plot displaying the DNA methylation level of the imprinted germline DMRs in *Padi6*$^{MatP620A/+}$ (*x*-axis) and *Padi6*$^{+/+}$ (*y*-axis) two-cell embryos, represented as in Figure 4J. (*K*) Upset plot intersecting the 2c-DEGs with promoter (TSS-3000+100) DNA methylation. The DEGs are divided into up-regulated and down-regulated; promoter DNA methylation is indicated as hypermethylated or hypomethylated if |methylation defect| > 10%. The data shown in *E–J* were analyzed using Wilcoxon signed ranked test. (ns) $P > 0.05$, (*) $P < 0.05$, (****) $P < 0.0001$.

active elements (Fig. 5I; Kozak 2015; Fu et al. 2019). In contrast, only slight and nonsignificant differences were found in the methylation of the imprinted DMRs (Fig. 5J; Supplemental Fig. S5C). Furthermore, comparison of whole-genome gene expression and DNA methylation revealed no significant correlation between differential gene expression and promoter methylation in the *Padi6*$^{MatP620A/+}$ embryos (Fig. 5K).

To distinguish whether the observed hypermethylation of the *Padi6*$^{MatP620A/+}$ two-cell embryo genome was likely to have resulted from de novo methylation or inefficient loss of gametic methylation, we compared the scBS-seq data of MII oocytes and two-cell embryos. This analysis took into account the distinct DNA methylation profiles of oocytes and sperm; notably, the bimodal pattern in oocytes with predominantly gene body methylation and unmethylated intergenic intervals, compared with the largely hypermethylated sperm genome. In addition, oocytes have a defined set of highly methylated CGIs, whereas CGIs are almost universally unmethylated in sperm (Smallwood et al. 2011; Kobayashi et al. 2012; Veselovska et al. 2015). Considering non-CGI tiles, we observed that the sequences that were methylated >80% (median = 96%) in the *Padi6*$^{+/+}$ MII oocytes had similar methylation levels (median = 95%) in the *Padi6*$^{P620A/P620A}$ oocytes (Fig. 6A; Supplemental Table S21). As expected from methylation reprogramming, these sequences were substantially demethylated (median = 66%) in the *Padi6*$^{+/+}$ two-cell embryos but largely maintained their methylation level (median = 90%) in the *Padi6*$^{MatP620A/+}$ two-cell embryos, consistent with a failure to demethylate the genome in the mutant embryos. Similarly, the sequences that were methylated <20% (median = 5%) in *Padi6*$^{+/+}$ oocytes but were likely hypermethylated in sperm maintained their

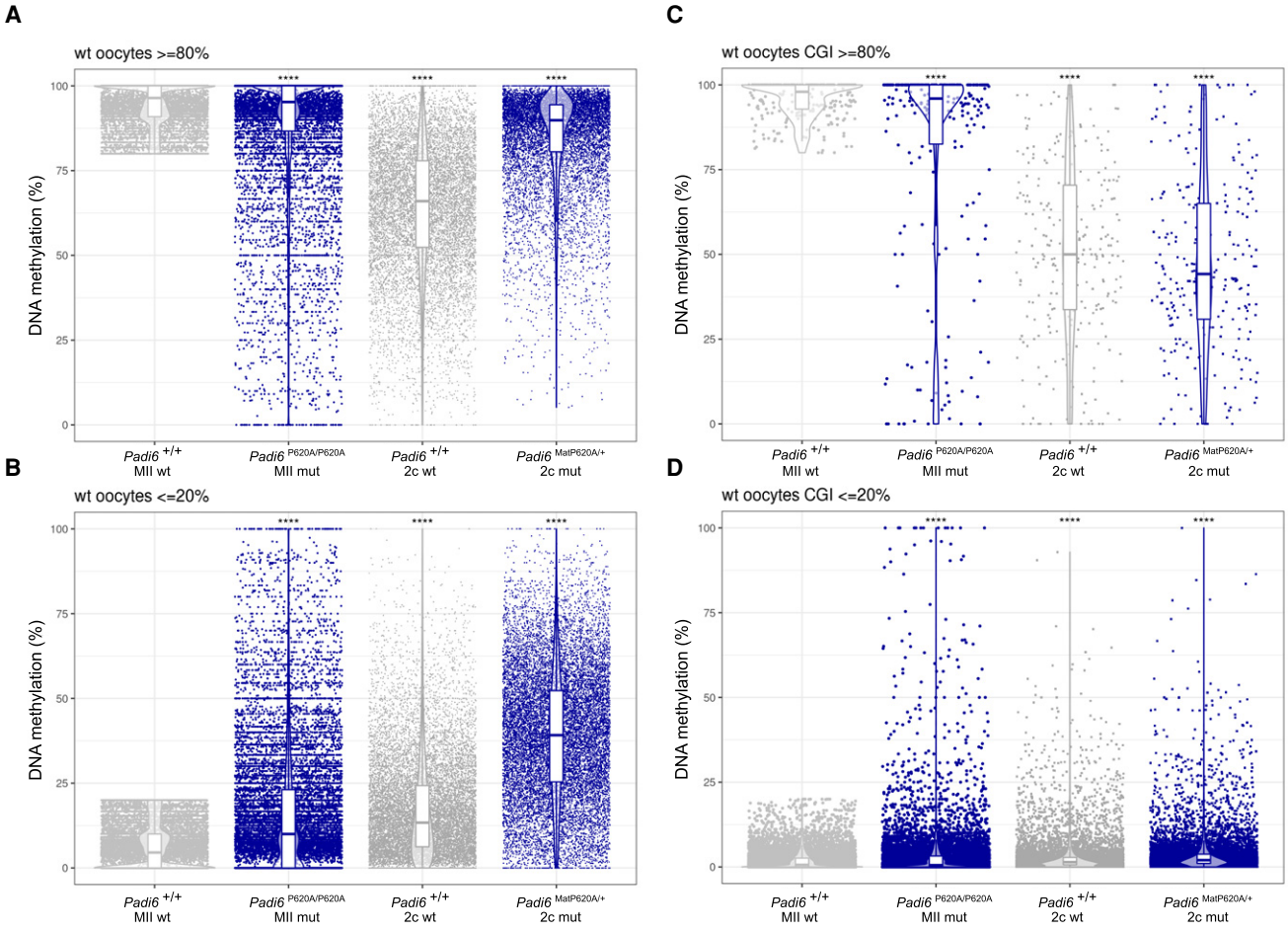

Figure 6. Comparison of methylation levels of MII oocytes and two-cell embryos. (*A*) Violin plots showing comparison of the average methylation of 100-CpG tiles (excluding CGIs) that are >80% methylated in *Padi6*$^{+/+}$ MII oocytes (MII wt) with the same tiles in *Padi6*$^{P620A/P620A}$ MII oocytes (MII mut), *Padi6*$^{+/+}$ two-cell embryos (2c wt), and *Padi6*$^{MatP620A/+}$ two-cell embryos (2c mut). (*B*) Analysis similar to *A* with tiles (excluding CGIs) that are <20% methylated in *Padi6*$^{+/+}$ MII oocytes. (*C*) Analysis similar to *A* with tiles covering CGIs that are >80% methylated in *Padi6*$^{+/+}$ MII oocytes. (*D*) Analysis similar to *A* with tiles covering CGIs that are <20% methylated in *Padi6*$^{+/+}$ MII oocytes. The lower methylation of some tiles in MII mut oocytes with respect to MII wt oocytes in *A* and *C* and the higher methylation in *B* and *D* are caused in part by hypomethylation of the mutant oocyte genome and in part by stochastic, sparse coverage and sampling of different CpGs in the tiles, as demonstrated by the reverse analysis (Supplemental Fig. S6). The data shown in *A*–*D* were analyzed using Wilcoxon signed ranked test. (****) $P < 0.0001$.

hypomethylated status in the *Padi6*$^{P620A/P620A}$ oocytes and *Padi6*$^{+/+}$ two-cell embryos (median = 10% and 13%, respectively) (Fig. 6B; Supplemental Table S21). However, these sequences were significantly more methylated (median = 39%) in the *Padi6*$^{MatP620A/+}$ embryos, again consistent with a failure of demethylating paternal DNA. Concerning CGIs, we found that those that were methylated >80% (median = 98%) in *Padi6*$^{+/+}$ MII oocytes and likely unmethylated in sperm maintained their methylation (median = 96%) in *Padi6*$^{P620A/P620A}$ oocytes but were similarly demethylated in *Padi6*$^{+/+}$ and *Padi6*$^{MatP620A/+}$ embryos (median = 50% and 44%, respectively) (Fig. 6C; Supplemental Table S22). Furthermore, the CGIs that were methylated <20% (median = 2%) in the *Padi6*$^{+/+}$ oocytes and likely similarly unmethylated in sperm mostly maintained their status in the *Padi6*$^{P620A/P620A}$ oocytes and *Padi6*$^{+/+}$ and *Padi6*$^{MatP620A/+}$ embryos (median = 1%, 1%, and 2%, respectively), suggesting that there is little or no de novo methylation detectable in the mutant embryos (Fig. 6D; Supplemental Table S22).

In summary, the *Padi6*$^{MatP620A/+}$ embryos were developmentally delayed at the two-cell stage with respect to wild type and failed to fully activate major ZGA genes and down-regulate Mat-decay genes at the two-cell stage. This gene dysregulation was accompanied by DNA hypermethylation that severely affected active LINEs and LTRs. Comparison between MII oocytes and two-cell embryos indicated that the relative hypermethylation of the mutant versus the wild-type embryos is the result of the failure of demethylation rather than a de novo event.

The PADI6^{P620A} *variant is associated with abnormal DNMT1 cellular localization*

To investigate the possible cause of the hypermethylation in the *Padi6*$^{MatP620A/+}$ two-cell embryos, we evaluated the expression levels of the DNA methylation-associated genes *Dnmt1*, *Dnmt3a*, *Tet3*, and *Uhrf1* using the scRNA-seq data set. No difference was found in expression of these genes between mutant and control MII oocytes or between mutant and control two-cell embryos (Fig. 7A,B). However, the protein level of UHRF1 was severely reduced (15-fold) in the mutant MII oocytes (Fig. 7C). Because DNMT1 activity is controlled through cytoplasm-to-nucleus transport during early development (Chen and Zhang 2020), we analyzed the subcellular localization of the proteins described above by immunofluorescence. We found that DNMT1 had the expected cytoplasmic localization in the *Padi6*$^{+/+}$ GV oocytes but was mostly concentrated in the nucleus of *Padi6*$^{P620A/P620A}$ GV oocytes (Fig. 7D). Notably, UHRF1, the DNMT1 accessory protein (Chen and Zhang 2020), also lost its normal cytoplasmic localization in *Padi6*$^{P620A/P620A}$ GV oocytes but did not appear to become as concentrated in the nucleus (Fig. 7E). In contrast to DNMT1 and UHRF1, the cellular localizations of both DNMT3A and TET3 were unaffected (Fig. 7F,G). A similar result was obtained in the zygotes. *Padi6*$^{MatP620A/+}$ zygotes showed a strong delocalization of DNMT1 and UHRF1 in both maternal and paternal pronuclei compared with *Padi6*$^{+/+}$ zygotes (Fig. 7H,I). In contrast, the subcellular localization of DNMT3A and TET3 was not altered (Fig. 7J, K). Taken together, these results demonstrate that DNMT1 was incorrectly localized in the nucleus in both *Padi6*$^{P620A/P620A}$ oocytes and *Padi6*$^{MatP620A/+}$ two-cell embryos, providing a possible explanation for the observed embryo hypermethylation.

To test whether genome hypermethylation was responsible for the developmental failure, we treated the embryos with the DNMT inhibitor 5-aza-2′-deoxycytidine (5-aza). We observed that the 5-aza treatment resulted in the reduction of 5mC level in the *Padi6*$^{MatP620A/+}$ two-cell embryos, as assessed by immunostaining (Fig. 8A,B). However, further development of either the *Padi6*$^{+/+}$ or *Padi6*$^{MatP620A/+}$ embryos was unaffected (Fig. 8C,D), suggesting that other mechanisms, possibly in addition to DNMT1 mislocalization, are responsible for the failure of preimplantation development in the *Padi6*$^{MatP620A/+}$ mutant.

Discussion

The integrity of the oocyte-derived SCMC-associated protein PADI6 is needed for preimplantation development in humans and mice, and *PADI6* variants are linked with imprinting disorders. In particular, PADI6 is needed for storing maternally supplied proteins on the cytoplasmic lattices in oocytes and for de novo transcription and translation in two-cell embryos (Yurttas et al. 2008, Jentoft et al. 2023). However, the mechanisms by which PADI6 controls these processes in early development are poorly defined. By applying single-cell analysis to a knock-in mouse line in which a BWS-associated *PADI6* variant was modeled, we provided functional insights into the mechanism by which the maternal *Padi6* gene controls epigenetic reprogramming and zygotic genome activation in preimplantation embryos.

Transcriptome analysis demonstrated down-regulation of many ZGA genes in the *Padi6*$^{MatP620A/+}$ two-cell embryos. Although both minor ZGA and major ZGA were found to be repressed, we noticed that the early two-cell markers *Duxf3* and *Duxbl1* (De Iaco et al. 2017) were normally expressed, while the DUX target genes *Zscan4c*, *Zscan4d*, *Zscan4f*, *Zfp352*, and *Trim43* (Geng et al. 2012; Sugie et al. 2020) were down-regulated in the *Padi6*$^{MatP620A/+}$ embryos, suggesting that the PADI6 variant mostly affected major ZGA in the late two-cell stage. Accordingly, further two-cell- and ZGA-specific genes (Genet and Torres-Padilla 2020), such as *Tcstv1*, *Tcstv3*, *Zfp352*, *Elf1a*, and *Wee1*, as well as several RNA polymerase genes, were found to be down-regulated. Analysis of cell cycle genes demonstrated that while the wild-type two-cell embryos were predominantly in G2/M, most of the mutant blastomeres were delayed in S phase, consistent with failure of late ZGA.

Failure of ZGA was accompanied by a dramatic hypermethylation of the whole genome in the *Padi6*$^{MatP620A/+}$ two-cell embryos with respect to their wild-type controls. Comparison between MII oocytes and two-cell embryos indicated that this was the result of a failure of demethylation rather than a de novo event in the

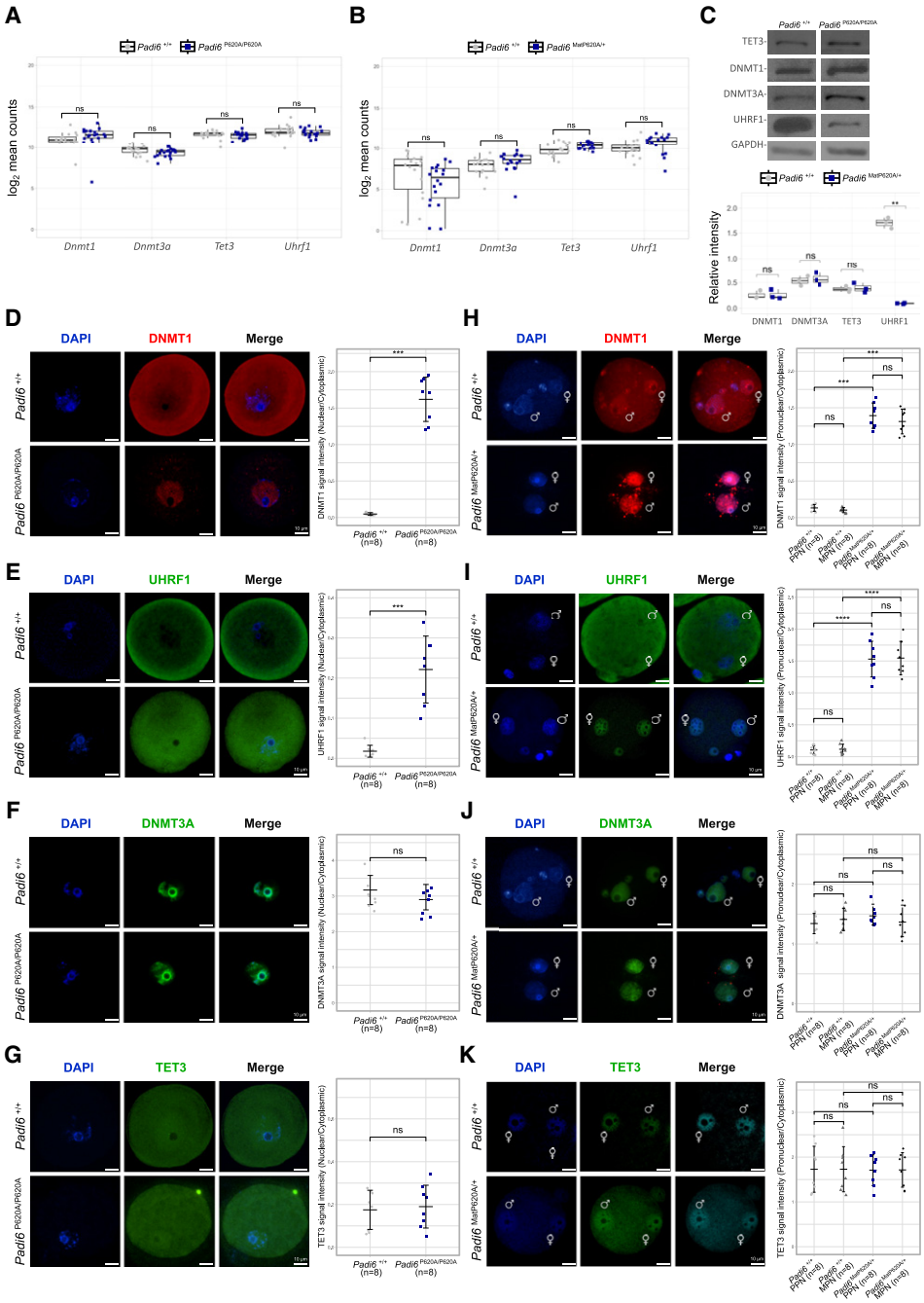

Figure 7. Effect of the *Padi6*^{P620A} variant on expression and subcellular localization of DNMTs, UHRF1, and TET3. (*A*) Box plot representing the expression level of the *Dnmt1*, *Dnmt3a*, *Tet3*, and *Uhrf1* genes, calculated as $\log_2$ mean counts of scRNA-seq data obtained from 18 *Padi6*$^{+/+}$ (gray) and 20 *Padi6*$^{P620A/P620A}$ (blue) MII oocytes. Each dot represents a single MII oocyte. (*B*) Box plot representing the expression level of the genes shown in *A* in 18 *Padi6*$^{+/+}$ (gray) and 18 *Padi6*$^{MatP620A/+}$ (blue) two-cell embryos. Each dot represents a single blastomere. (*C*, *top*) Western blot analysis of TET3, DNMT1, DNMT3A, UHRF1, and GAPDH in *Padi6*$^{+/+}$ and *Padi6*$^{P620A/P620A}$ oocytes. (*Bottom*) Quantification of protein signal intensity normalized on GAPDH. (*D–G*, *left*) Representative images of *Padi6*$^{+/+}$ (*top*) and *Padi6*$^{P620A/P620A}$ (*bottom*) GV oocytes immunostained with anti-DNMT1 (red; *D*), anti-UHRF1 (green; *E*), anti-DNMT3A (green; *F*), and anti-TET3 (green; *G*) antibodies. (*Right*) Quantification of the DNMT1 (*D*), UHRF1 (*E*), DNMT3A (*F*), and TET3 (*G*) nuclear/cytoplasmic ratio in *Padi6*$^{+/+}$ and *Padi6*$^{P620A/P620A}$ GV oocytes. (*H–K*, *left*) Representative images of *Padi6*$^{+/+}$ (*top*) and *Padi6*$^{MatP620A/+}$ (*bottom*) zygotes immunostained with anti-DNMT1 (red; *H*), anti-UHRF1 (green; *I*), anti-DNMT3A (green; *J*), and anti-TET3 (green; *K*) antibodies. The maternal (MPN) and paternal (PPN) pronuclei are indicated by ♀ and ♂, respectively. (*Right*) Quantification of the DNMT1 (*H*), UHRF1 (*I*), DNMT3A (*J*), and TET3 (*K*) pronuclear/cytoplasmic ratio in *Padi6*$^{+/+}$ and *Padi6*$^{MatP620A/+}$ zygotes. (*D–K*) "*n*" denotes the number of oocytes analyzed in three independent experiments. The data in *A–K* are mean ± SD and were analyzed using an unpaired two-tailed Student's *t*-test. (ns) $P > 0.05$, (**) $P < 0.01$, (***) $P < 0.001$, (****) $P < 0.0001$. *C–K* are representative images from three independent biological replicates.

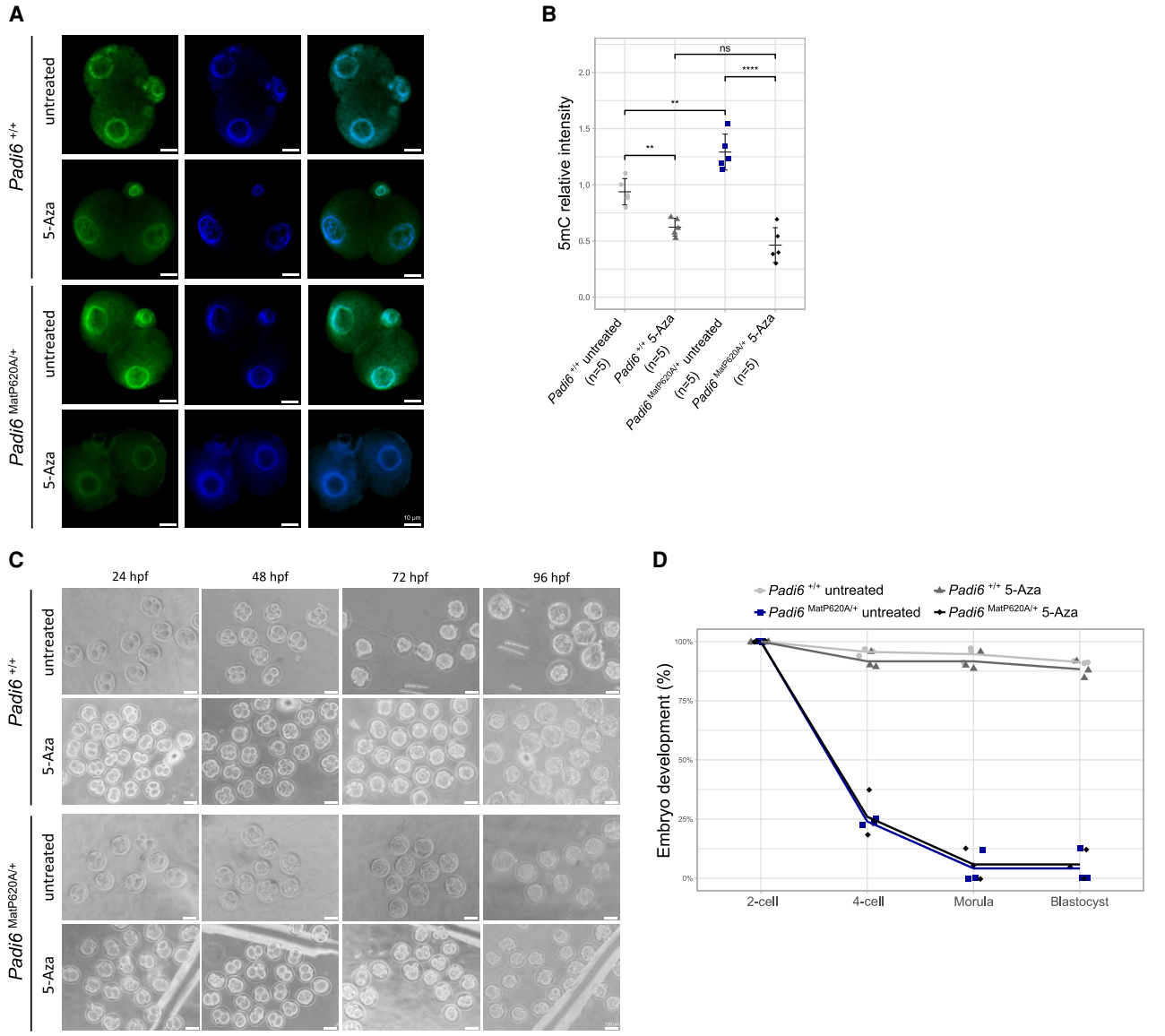

Figure 8. Effect of 5-aza treatment on *Padi6*$^{+/+}$ and *Padi6*$^{MatP620A/+}$ two-cell embryos. (*A*) Immunostaining with anti-5mC antibodies of *Padi6*$^{+/+}$ and *Padi6*$^{MatP620A/+}$ two-cell embryos untreated or treated with the methylation inhibitor 5-aza. (*B*) Quantification of the immunofluorescent signal of 5mC after the 5-aza treatment in both wt and mutant two-cell embryos. "*n*" in parentheses denotes the number of oocytes analyzed in three independent experiments (*C*) Representative still frames of *Padi6*$^{+/+}$ and *Padi6*$^{MatP620A/+}$ embryos untreated or treated with 5-aza at 24, 48, 72, and 96 h after IVF. (*D*) Line plot showing the percentage of *Padi6*$^{+/+}$ embryos untreated (gray) or treated with 5-aza (dark gray) and *Padi6*$^{MatP620A/+}$ embryos untreated (blue) or treated with 5-aza (black), developed after IVF. Each dot represents an independent experiment.

mutant embryos. The hypermethylation involved gene promoters, but no correlation was found between gene methylation and expression. Repetitive elements, in particular LTRs and LINEs, were hypermethylated as well. It has been demonstrated that DUX activates transcription of MERVL retrotransposons and that this is required for development beyond the two- to four-cell stage (Hendrickson et al. 2017; Sakashita et al. 2023). In addition, several two-cell genes, such as *Zscan4*$^{-}$, *Tcstv1/3*, *Eif1a*, *Tho4* (*Gm4340*), *Tdpoz*$^{-}$, and *Zfp352*, which we found down-regulated in the *Padi6*$^{MatP620A/+}$ embryos, are transcribed as chimeric genes with MERVL LTRs (Macfarlan et al. 2012). Concerning the LINEs, it has been shown that their activation at the two-cell stage regulates global chromatin accessibility, and their targeted repression strongly affects development rate (Jachowicz et al. 2017). Interestingly, we found that the more recently evolved LTRs and LINEs that retain transcription had the most highly significant gain of methylation. DNA methylation is required to maintain repression of ERV and LINE transposons in postimplantation embryos (Dahlet et al.

2020; Graham-Paquin et al. 2023), suggesting that hypermethylation may interfere with their timely activation and ZGA in early embryos.

In preimplantation embryos, DNMT1 and its cofactor, UHRF1, are actively retained in the cytoplasm, thus enabling demethylation of the genome by passive dilution at DNA replication (Cardoso and Leonhardt 1999; Maenohara et al. 2017). In contrast, we found that DNMT1 and UHRF1 are mostly concentrated in the pronuclei of the *Padi6*$^{MatP620A/+}$ zygotes. The aberrant nuclear localization of DNMT1 and UHRF1 was already evident in *Padi6*$^{P620A/P620A}$ GV oocytes, indicating that this precedes the impaired demethylation and ZGA of the mutant two-cell embryos. In addition, the protein level of UHRF1 was severely reduced in the mutant GV oocytes. We did not find DNA hypermethylation in the *Padi6*$^{P620A/P620A}$ MII oocytes despite the strong nuclear staining of DNMT1, but perhaps the apparently more limited nuclear presence of UHRF1 prevents excessive methylation. The mechanism by which PADI6 controls intracellular DNMT1 and UHRF1 localization remains elusive. However, DNMT1 was also found in the nuclei of *Nlrp2*/*Stella*, *Nlrp14*/*Stella* and *Pgc7*/*Stella* maternal knockout embryos, all of which showed cytoplasmic defects (Mahadevan et al. 2017; Li et al. 2018; Meng et al. 2023; Yan et al. 2023). Furthermore, *Nlrp14*/*Stella* and *Pgc7*/*Stella* maternal knockout embryos displayed genomic hypermethylation and ZGA failure. Jentoft et al. (2023) demonstrated that UHRF1 is enriched on cytoplasmic lattices in oocytes, suggesting that PADI6 may contribute to retention of this protein and, indirectly, of DNMT1 in the cytoplasm. Interestingly, we also found that the subcellular localization of OOEP that has been reported to interact with PADI6 (Li et al. 2008), but not that of NLRP5 and TLE6, was changed in the mutant oocytes. Treatment of our mutant embryos with 5-aza reverted the hypermethylation but did not rescue the developmental failure, indicating that the incomplete demethylation is due to nuclear localization of DNMT1 but that other mechanisms are responsible for the developmental arrest in our mutant mice.

After fertilization, the zygotic genome is inert, and mRNAs derived from the oocyte are translated to direct embryo development up to the two-cell stage (Chen et al. 2023). Oocyte transcripts are progressively decayed through either maternal (Mat-decay) and zygotic (Z-decay) pathways (Jiang and Fan 2022; Chen et al. 2023). In particular, the Z-decay pathway involves the polyA-binding proteins PABPC1 and PABPN1, both of which were found to be down-regulated at the transcriptional level in *Padi6*$^{MatP620A/+}$ embryos, suggesting that the up-regulation of Mat-decay genes is a consequence of the ZGA failure or developmental delay of the mutant embryos. Additional factors, such as *Btg4* (Zheng et al. 2020), which is slightly down-regulated, may be involved in the deregulation of Z-decay in the *Padi6*$^{MatP620A/+}$ embryos.

Although no significant difference in ovulation efficiency was observed between the *Padi6*$^{P620A/P620A}$ and *Padi6*$^{+/+}$ mouse lines, the mutant MII oocytes displayed evidence of maturation defects with an increase of cells characterized by abundance of GV-specific markers and genes involved in cytoplasmic and metabolic processes. These molecular changes, which affect crucial processes of oocyte maturation, may interfere with embryonic development. PADI6 also interacts with the maternal-effect zygotic arrest-1 (ZAR1) protein, which is involved in oocyte maturation by interacting with cytoplasmic lattices and controlling mRNA stability and translation, which may be affected in the *Padi6*$^{P620A/P620A}$ oocytes (Rong et al. 2019). However, it should also be taken into account that in our study, the MII oocytes were collected after PMSG + hCG stimulation that may have pushed immature oocytes to ovulate (Moor et al. 1985) and enhanced the difference between the mutant and the control oocytes.

In silico studies predicted that the mouse P620A is more destabilizing than the human P632A variant on the PADI6 structure, possibly due to interference with a stabilizing hydrophobic Met–Phe interaction that is present only in the mouse protein. Consistent with this observation, *Padi6*$^{P620A/P620A}$ female mice were infertile, while a woman carrying the *PADI6*^{P632A} variant in compound heterozygosity with a null mutation conceived two children with BWS and MLID and did not report any fertility problem (Cubellis et al. 2020). So, the phenotype associated with the mouse *Padi6*^{P620A} variant is more severe than that associated with the orthologous human variant. Despite the reduction in UHRF1 protein levels in the mutant oocytes, we did not find any significant change in the methylation of the imprinted DMRs in either mutant oocytes or two-cell embryos. This is consistent with the findings obtained with the *Nlrp2* and *Nlrp14* knockout mouse lines, in which minor and no imprinting defects were reported (Mahadevan et al. 2017; Yan et al. 2023). In addition, the similar methylation profiles of the *Padi6*$^{P620A/P620A}$ and *Padi6*$^{+/+}$ MII oocytes indicates that, at least in mice, PADI6 is not required for de novo methylation, as demonstrated for human KHDC3L (Demond et al. 2019). Some redundancy in the human SCMC proteins (e.g., NLRP7 is absent in mice) or differences in ZGA length may explain these phenotypic differences between humans and mice. Because our analysis was limited to the two-cell stage, it is possible that the embryos surviving the impaired ZGA may develop defects in maintenance of imprinted methylation after the two-cell stage.

In conclusion, our study provides further insights into the function of the maternal-effect gene *Padi6* in early mouse development. Our data are consistent with a model in which PADI6, likely within the cytoplasmic lattices, controls oocyte maturation and storage of maternal proteins including UHRF1 and DNMT1 in the oocyte cytoplasm. Loss of these functions due to *Padi6* inactivation leads to failure of epigenetic reprogramming and ZGA, as well as developmental arrest at the two-cell stage.

Materials and methods

Generation of the Padi6^{P620A} *mouse line*

The P620A variant was introduced into the *Padi6* locus of E14Tg2a4 (129/SV) ESCs by homologous recombination.

Homology arms obtained from a BAC clone containing Padi6 isogenic DNA were inserted into a pFLRT3D vector modified for Flp/Frt-based recombination. Details of the targeting strategy are available on request. The linearized targeting vector was electroporated into ESCs, and upon G418 selection, three positive clones were identified by PCR and confirmed by Southern blotting with one internal and two external probes. The presence of the mutation was assessed by allele-specific PCR. In order to generate chimeras, 10–15 ESCs from one clone were microinjected into C57Bl/6 blastocysts, and 10 blastocysts were reimplanted in each uterine horn of pseudopregnant B6D2 females after they were anaesthetized with 80 mg/kg ketamine and 10 mg/kg xylazine. Highly chimeric animals were crossed to Flp recombinase deleter mice to remove the neomycin cassette. The offspring were used to establish the *Padi6*^{P620A} mouse colony. All experimental procedures involving animals were conducted according to authorization number 830/2020-PR, released by the Italian Ministry of Health. The primers used are listed in Supplemental Table S23. The transgenic Padi6P620A line has been generated by the Mouse Modeling Facility of the Institute of Genetics and Biophysics A. Buzzati-Traverso, Consiglio Nazionale delle Ricerche.

Mouse genotyping

The presence of the *Padi6* variant, the removal of the Neo box, and the presence of the flippase gene were demonstrated by PCR on tail DNA extracted with standard procedures. Amplicons of 430 and 290 bp were amplified from the mutant or wild-type *Padi6* alleles, respectively, using the primers Padi6_RimF and Padi6_RimR. This difference was due to a fragment of the Neo box remaining after the flippase recombination. The presence of the mutation was also identified by digestion with the restriction enzyme StuI, which was generated by the mutation after amplification of a 420-bp fragment with the primers forward LA HindIII + SnaBI and reverse GEN Padi6. The presence of the Neo box was detected using the primers PGK1A forward and Padi6_RimR. The presence of the flippase was detected using the primers FLP_F and FLP_R. The primer sequences are listed in Supplemental Table S23.

Assessment of fertility

Two-month-old to 4-mo-old female *Padi6*$^{+/+}$, *Padi6*$^{+/P620A}$, or *Padi6*$^{P620A/P620A}$ mice were housed with >8-wk-old *Padi6*$^{+/+}$ male mice from 4:00 p.m. to 6:00 p.m. and checked for the presence of vaginal plugs the next morning. Positive females were monitored for pregnancy and delivery.

MII oocyte collection, in vitro fertilization, and embryo treatment with 5-aza-2′-deoxycytidine

Heterologous in vitro fertilization was performed according to the method described by Taft (2017). Eight-week-old to 12-wk-old males and 4- to 8-wk-old females were used. To induce superovulation, the females received intraperitoneal injections of pregnant mare serum gonadotropin (PMSG) on day 1 at 2:00 p.m. and human chorionic gonadotropin (hCG) after 52 h. Males were sacrificed ~12 h after the female hCG injection, the cauda epididymis and vasa deferentia were dissected, and spermatozoa were collected in human tubal fluid (HTF) medium (EmbryoMax HTF MR-070-D). Spermatozoa were counted and incubated at 37°C in a humidified atmosphere with 5% CO_2. Females were sacrificed 13 h after the hCG injection. Ampullae were placed in 1 mg/mL hyaluronidase drops (H6254-500MG) to break down the oocyte–cumulus complex and collect MII oocytes. The oocytes were moved to the HTF medium, and spermatozoa were added at a concentration of 2×10^6 sperm/mL. After 4–6 h of incubation at 37°C, the fertilized oocytes were washed to remove spermatozoa and debris, transferred to KSOM medium, and incubated overnight at 37°C. The embryos' status was evaluated the next morning and over the following 120 h. To inhibit DNMTs and reduce DNA methylation, embryos were cultured in KSOM containing 50 nM 5-aza-2′-deoxycytidine (Sigma-Aldrich A3656) for 0–96 h following IVF.

DNA and RNA isolation for single-cell genomic analysis

MII oocytes and two-cell embryos were individually lysed, flash-frozen in 5 µL of RLT Plus buffer (Qiagen), and stored at −80°C until further use. For two-cell embryos, the zona pellucida was removed with Tyrode's solution (Sigma-Aldrich), blastomeres were separated, and the polar body was discarded. DNA and RNA were separated using the G&T protocol (Angermueller et al. 2016). Magnetic beads (MyOne C1, Life Technologies) were washed and annealed to oligo dTs and then used to capture polyadenylated mRNA from individual cell lysates. The supernatant containing the DNA was transferred to a new tube, and the beads washed three times in 1× FSS buffer (SuperScript II, Invitrogen), 10 mM DTT, 0.005% Tween-20 (Sigma), and 0.4 U/µL RNasin (Promega) to remove all DNA residues. Each washing solution was added to the DNA tube to maximize recovery.

Construction of scBS-seq libraries

The scBS-seq libraries were generated as described (Clark et al. 2017). The DNA was purified from the lysate using a 0.9:1 ratio of Ampure XP beads (Beckman Coulter) and eluted into 10 µL of water. DNA purified from single cells was treated with the EZ Methylation Direct kit (Zymo) for bisulfite conversion following the manufacturer's instructions. First-strand synthesis was performed in five rounds. Initially, the bisulfite-treated DNA was mixed with 40 µL of first-strand synthesis master mix (1× blue buffer [Enzymatics], 0.4 mM dNTP mix [Roche], 0.4 µM 6NF oligo [IDT]), heated for 2 min to 65°C, and cooled on ice, followed by the addition of 50 U of exo$^-$ Klenow fragment DNA polymerase (Enzymatics) and incubation for 30 min at 37°C after slowly ramping up from 4°C. This process was repeated four more times, with additional reaction mixture added each time, and the final round was

incubated for 90 min at 37°C. Exonuclease digestion was carried out by adding 20 U of exonuclease I (NEB) in a total volume of 100 µL for 1 h at 37°C. The resulting samples were purified using AMPure XP beads with a 0.8:1 ratio. The beads were mixed with 50 µL of second-strand master mix (1× blue buffer [Enzymatics], 0.4 mM dNTP mix [Roche], 0.4 µM 6NF oligo [IDT]). The mixture was heated for 1 min to 98°C and then cooled on ice. Next, 50 U of exo$^-$ Klenow was added. The mixture was incubated on a thermocycler for 90 min at 37°C after slowly ramping up from 4°C. The resulting samples were purified using a 0.8:1 ratio of AMPure XP beads, and libraries were amplified using 50 µL of PCR master mix (1× KAPA HiFi Readymix, 0.2 µM PE1.0 primer, 0.2 µM iTAG index primer). The amplification process involved a 2-min step at 95°C, followed by 14 cycles of 80 sec at 94°C, 30 sec at 65°C, and 30 sec at 72°C, with a final extension of 3 min at 72°C. Finally, the scBS-seq libraries were subjected to purification using a 0.7:1 ratio of AMPure XP beads. After purification, the libraries were eluted in 15 µL of water, pooled together, and sequenced. The sequencing process involved the generation of pools of 48 libraries, which were sequenced on an Illumina HiSeq 2500 platform. On average, the libraries were sequenced to generate 13.0 million paired-end reads with a read length of 75 bp.

Construction of scRNA-seq libraries

The mRNA bound to the beads was processed further for cDNA conversion. This involved the resuspension of the beads in 10 µL of reverse transcriptase master mix (100 U of SuperScript II [Invitrogen], 10 U of RNasin [Promega], 1× Superscript II first-strand buffer, 5 mM DTT [Invitrogen], 1 M betaine [Sigma], 9 mM $MgCl_2$ [Invitrogen], 1 µM template-switching oligo [TSO; Eurogentec], 1 mM dNTP mix [Roche]). The mRNA mixture was reverse-transcribed by incubation for 60 min at 42°C followed by 30 min at 50°C and 10 min at 60°C. The cDNA obtained was subjected to PCR amplification by adding 11 µL of 2× KAPA HiFi HotStart ReadyMix and 1 µL of 2 µM ISPCR primer. The amplification was performed in a thermocycler for 3 min at 98°C, followed by 15 cycles of 15 sec at 98°C, 20 sec at 67°C, and 6 min at 72°C, and a final extension step of 5 min at 72°C. The amplified product was purified using Ampure XP beads with a 1:1 ratio and eluted into 20 µL of water. Libraries were prepared from 100–400 pg of cDNA using the Nextera XT kit (Illumina) following the manufacturer's instructions but with one-fifth volumes. All 96 single-cell RNA-seq libraries were pooled together and sequenced on an Illumina NextSeq platform to an average depth of 4.2 million reads using paired-end 75-bp read length settings.

Histological analysis

Ovaries were collected from 2- to 4-mo-old mice, fixed in formalin overnight, dehydrated through graded alcohol solutions, and immersed in xylene for 1 h for diaphanization. They were finally embedded in paraffin blocks and cut with a rotary microtome (Leica RM2235) into 7-µm-thick sections, which were mounted onto glass slides. Next, they were deparaffinized in xylene, rehydrated through graded alcohol solutions, and stained with hematoxylin and eosin (H&E). The H&E images of the ovaries were captured using a Nikon motorized optical microscope.

Immunostaining of mouse tissues, oocytes, and zygotes

GV oocytes, zygotes, and two-cell embryos were fixed with 4% paraformaldehyde in PBS for 30 min at room temperature and washed three times with PBS. Fixed cells were incubated in the permeabilization solution (0.5% Triton X-100 in PBS) for 30 min. After incubation with a blocking solution (0.1% BSA, 0.05% Tween-20 in PBS) for 1 h at room temperature, the cells were incubated overnight at 4°C with the primary antibody. After three washes, the cells were incubated with the secondary antibody for 1 h at room temperature. For detection of 5mC, two-cell embryos were treated with 4 M HCl for 10 min at room temperature and then neutralized for 10 min with 100 mM Tris-HCl (pH 7.5). Ovarian tissue sections were processed as described for the histological analysis, until deparaffinization and rehydration. Antigen retrieval was performed by microwave processing at 700 W in 0.01 M citrate buffer (pH 6.0) for 10 min. Slides were incubated with blocking solution (0.5% milk, 10% FBS, 1% BSA in H_2O, 0.02% NaN_3) for 60 min at room temperature in a humidified chamber, and the same blocking solution was used to dilute primary and secondary antibodies. The slides were incubated in humidified conditions overnight at 4°C after addition of the primary antibody and for 1 h at room temperature after addition of the secondary antibody. Cells and tissues were mounted in SlowFade Gold antifade reagent with DAPI (S36938) and observed using a Nikon motorized optical microscope with a 20× ocular lens. The following primary antibodies were used in this study: anti-PADI6 (1:500; S. Coonrod's laboratory), anti-OOEP (1:200; PA586033), anti-DNMT1 (1:250; ab13537), anti-DNMT3A (1:500; ab188470), anti-TET3 (1:400; NBP2-20602), and anti 5mC (1:500; C15200081-100). Secondary antibodies used in this study were anti-mouse Alexa fluor 594 (1:1000; A11032), antirabbit Alexa fluor 448 (1:500; A11008), and anti-guinea pig Alexa fluor 594 (1:500; A11076).

RNA analysis

RNA was isolated from ovaries using the TRI reagent (Sigma-Aldrich) according to the manufacturer's instructions. Approximately 900 ng of total RNA was retrotranscribed using the QuantiTect reverse transcription kit (Qiagen) according to the manufacturer's protocol. For locus-specific gene expression analysis, cDNA was amplified by real-time PCR using SYBR Green PCR master mix (Bio-Rad) on a CFX Connect real-time PCR detection system. The primers used are listed in Supplemental Table S23.

Western blotting

Tissues were resuspended in RIPA buffer (50 mM Tris HCl at pH 7.5, 150 mM NaCl, 1 mM EDTA, 1% Triton X-100), homogenized with the tissue lyser, and incubated for 30 min at 4°C. Proteins were quantified by Quick Start Bradford protein assay (Bio-Rad). The proteins for Western blotting were boiled for 10 min at 95°C in Laemmli buffer and resolved by 8% acrylamide gel. Samples were transferred onto nitrocellulose membranes (Bio-Rad Transblot) and processed using standard procedures. Signals were visualized using an ECL method. For the GV oocyte protein extraction, a total number of 50 GV oocytes was directly lysed in Laemmli sample buffer containing protease inhibitor, heated for 10 min at 95°C, and then processed using standard procedures. ImageJ software was used to quantify the bands. The primary antibodies used were anti-PADI6 (1:1000), anti-NLRP5 (1:500; sc514988), and anti-TLE6 (1:1000; sc515065). The secondary antibodies used were antimouse (1:10,000; ab6728), antirabbit (1:10,000; ab6721), and anti-guinea pig (1:5000; ab6908).

Processing of scRNA-seq data

A total of 96 libraries was adapted and quality-trimmed (Phred score <20) using Trim Galore version 0.4.4 (https://www.bioinformatics.babraham.ac.uk/projects/trim_galore). We also sequenced four negative controls to archive technical problems. The good quality reads were aligned to the Genome Reference Consortium mouse genome build 39 (GRCm39) with HiSat2 version 2.1.0 (Kim et al. 2015) in paired-end mode. The data were quantified in SeqMonk and analyzed in Rstudio (Supplemental Tables S24, S25). The count matrix was used to calculate the differential expression following the DESeq2 pipeline (Love et al. 2014). The list of ZGA and maternal decay genes was imported into the STRING database (Jensen et al. 2009). Cluster analysis was performed using the "kmean clustering" option with "number of clusters" parameter set to 4. The edges between clusters were set as "dotted line." To explore the processes in which those proteins are involved, we used gprofiler2 (Kolberg et al. 2020) with default options. To infer the cell cycle phase, we used the CellCycleScoring function in Seurat package v4.4.0 (Hao et al. 2023).

Processing of scBS-seq data

A total of 96 scBS-seq libraries was processed for analysis. The first 6 bp containing the N portion of the random primers, adapters, and bases called with poor quality (Phred score <20) were removed using Trim Galore version 0.4.4 (https://www.bioinformatics.babraham.ac.uk/projects/trim_galore) in single-end mode. Only the good quality reads were used for alignment to the Genome Reference Consortium mouse genome build 39 (GRCm39) using Bismark version 0.18.2 (Krueger and Andrews 2011) with single-end and nondirectional mode followed by deduplication and methylation calling using Bismark functions. The MII scBS-seq libraries with a mapping efficiency <10% or <500,000 CpGs covered were removed; in addition, to exclude samples with likely somatic DNA contamination, we removed samples with an X-chromosome CpG island mean methylation of >12.5% (Supplemental Table S26; Castillo-Fernandez et al. 2020), and there was no difference in the proportion of oocytes excluded on this basis between *Padi6*$^{P620A/P620A}$ and control samples. In total, out of 44 MII oocytes, we kept six cells for downstream analysis. Embryo scBS-seq libraries with <100,000 reads were removed. In total, out of 44 embryos, we kept 29 samples for downstream analysis (Supplemental Table S27). The methylation profile for each feature was calculated by the bisulfite methylation pipeline implemented in SeqMonk. To assess the global methylation differences among the mutant and wild-type cells, we calculated 100-CpG tiles defined using SeqMonk. The CpGI and Rmsk tracks were downloaded from UCSC Genome Browser and converted to mm39 coordinates using the liftOver tool. The gene body, the promoter (gene upstream −3000 + 100), and the other methylation features were quantitated with the bisulfite pipeline in SeqMonk. The coordinates for imprinted DMRs were used to quantitate the methylation in both MII oocytes and embryos (Supplemental Table S28).

Whole-genome sequencing

Whole-genome sequencing was performed on genomic DNA extracted from the tail of a homozygous *Padi6*$^{P620A/P620A}$ female. The DNA samples were sequenced with 150-bp paired ends at Biodiversa srl Service using Illumina Nextera DNA preparation and the Illumina NovaSeq6000 platform. The bioinformatic analysis was performed as previously reported. The read quality was checked using FASTQC tools (http://www.bioinformatics.babraham.ac.uk/projects/fastqc). Reads were aligned to the mouse genome reference assembly (mm39) using BWAmem software package v0.7.17 (Li and Durbin 2009). PCR duplicates were filtered out using Picard v2.9 (http://picard.source forge.net) and Dellytools v1.1.6 (Rausch et al. 2012) with default parameters used to calculate the structural variants and CNVs.

Analysis of protein structural models

Structural models of human and mouse PADI6 (https://alphafold.ebi.ac.uk/entry/Q6TGC4 and https://alphafold.ebi.ac.uk/entry/Q8K3V4) were obtained from the AlphaFold Protein Structure Database (Varadi et al. 2022). Secondary structure assignment was performed using SEGNO (Cubellis et al. 2005). Prediction of mutant protein stability was performed using the DynaMut suite (Rodrigues et al. 2018). Analysis of models and picture production were done using Chimera (Pettersen et al. 2004).

Availability of data and materials

Raw data supporting the findings of this study have been deposited under accession number GSE245426 in the Gene Expression Omnibus repository.

Competing interest statement

The authors declare no competing interests.

Acknowledgments

We thank Megan Hamilton of the Babraham Genomics Facility for support with sequencing. This work was supported by grants from the Associazione Italiana Ricerca sul Cancro (AIRC; IG 2020 ID 24405) and Telethon (GMR23T1062) to A.R. Work in G.K.'s laboratory was funded by the UK Biotechnology and Biological Sciences Research Council (BBS/E/B/000C0423), Medical Research Council (MR/K011332/1 and MR/S000437/1), and the Wellcome Trust (210754/B/18/Z).

Author contributions: C.G., F. Cecere, D.A., F. Cerrato, S. Cecconi, G.K., and A.R. designed experiments and interpreted results. C.G., L.A., A.P., D.A., B.A., G.R., and S. Cecconi performed experiments. F. Cecere., C.G., B.H.M., M.V.C., A.G., and S.A. performed bioinformatic analyses. B.H.M. carried out the analysis of protein structure models. S. Coonrod provided homemade reagents that were necessary for performing experiments. C.G., F. Cecere, and A.R. wrote the manuscript with input from all authors.

References

Angermueller C, Clark SJ, Lee HJ, Macaulay IC, Teng MJ, Hu TX, Krueger F, Smallwood S, Ponting CP, Voet T, et al. 2016. Parallel single-cell sequencing links transcriptional and epigenetic heterogeneity. *Nat Methods* **13:** 229–232. doi:10.1038/nmeth.3728

Anvar Z, Chakchouk I, Sharif M, Mahadevan S, Nasiotis ET, Su L, Liu Z, Wan YW, Van den Veyver IB. 2023. Loss of the maternal effect gene Nlrp2 alters the transcriptome of ovulated mouse oocytes and impacts expression of histone demethylase KDM1B. *Reprod Sci* **30:** 2780–2793. doi:10.1007/s43032-023-01218-8

Aoki F. 2022. Zygotic gene activation in mice: profile and regulation. *J Reprod Dev* **68:** 79–84. doi:10.1262/jrd.2021-129

Barlow DP, Bartolomei MS. 2014. Genomic imprinting in mammals. *Cold Spring Harb Perspect Biol* **6:** a018382. doi:10.1101/cshperspect.a018382

Bebbere D, Albertini DF, Coticchio G, Borini A, Ledda S. 2021. The subcortical maternal complex: emerging roles and novel perspectives. *Mol Hum Reprod* **27:** gaab043. doi:10.1093/molehr/gaab043

Cardoso MC, Leonhardt H. 1999. DNA methyltransferase is actively retained in the cytoplasm during early development. *J Cell Biol* **147:** 25–32. doi:10.1083/jcb.147.1.25

Castillo-Fernandez J, Herrera-Puerta E, Demond H, Clark SJ, Hanna CW, Hemberger M, Kelsey G. 2020. Increased transcriptome variation and localised DNA methylation changes in oocytes from aged mice revealed by parallel single-cell analysis. *Aging Cell* **19:** e13278. doi:10.1111/acel.13278

Chen Z, Zhang Y. 2020. Role of mammalian DNA methyltransferases in development. *Annu Rev Biochem* **89:** 135–158. doi:10.1146/annurev-biochem-103019-102815

Chen Y, Wang L, Guo F, Dai X, Zhang X. 2023. Epigenetic reprogramming during the maternal-to-zygotic transition. *MedComm (2020)* **4:** e331.

Clark SJ, Smallwood SA, Lee HJ, Krueger F, Reik W, Kelsey G. 2017. Genome-wide base-resolution mapping of DNA methylation in single cells using single-cell bisulfite sequencing (scBS-seq). *Nat Protoc* **12:** 534–547. doi:10.1038/nprot.2016.187

Cubellis MV, Cailliez F, Lovell SC. 2005. Secondary structure assignment that accurately reflects physical and evolutionary characteristics. *BMC Bioinformatics* **6 Suppl 4:** S8. doi:10.1186/1471-2105-6-S4-S8

Cubellis MV, Pignata L, Verma A, Sparago A, Del Prete R, Monticelli M, Calzari L, Antona V, Melis D, Tenconi R, et al. 2020. Loss-of-function maternal-effect mutations of PADI6 are associated with familial and sporadic Beckwith-Wiedemann syndrome with multi-locus imprinting disturbance. *Clin Epigenetics* **12:** 139. doi:10.1186/s13148-020-00925-2

Dahlet T, Argüeso Lleida A, Al Adhami H, Dumas M, Bender A, Ngondo RP, Tanguy M, Vallet J, Auclair G, Bardet AF, et al. 2020. Genome-wide analysis in the mouse embryo reveals the importance of DNA methylation for transcription integrity. *Nat Commun* **11:** 3153. doi:10.1038/s41467-020-16919-w

De Iaco A, Planet E, Coluccio A, Verp S, Duc J, Trono D. 2017. DUX-family transcription factors regulate zygotic genome activation in placental mammals. *Nat Genet* **49:** 941–945. doi:10.1038/ng.3858

Demond H, Anvar Z, Jahromi BN, Sparago A, Verma A, Davari M, Calzari L, Russo S, Jahromi MA, Monk D, et al. 2019. A KHDC3L mutation resulting in recurrent hydatidiform mole causes genome-wide DNA methylation loss in oocytes and persistent imprinting defects post-fertilisation. *Genome Med* **11:** 84. doi:10.1186/s13073-019-0694-y

Eggermann T, Yapici E, Bliek J, Pereda A, Begemann M, Russo S, Tannorella P, Calzari L, de Nanclares GP, Lombardi P, et al. 2022. *Trans*-acting genetic variants causing multilocus imprinting disturbance (MLID): common mechanisms and consequences. *Clin Epigenetics* **14:** 41. doi:10.1186/s13148-022-01259-x

Eggermann T, Monk D, de Nanclares GP, Kagami M, Giabicani E, Riccio A, Tümer Z, Kalish JM, Tauber M, Duis J, et al. 2023. Imprinting disorders. *Nat Rev Dis Primers* **9:** 33. doi:10.1038/s41572-023-00443-4

Esposito G, Vitale AM, Leijten FP, Strik AM, Koonen-Reemst AM, Yurttas P, Robben TJ, Coonrod S, Gossen JA. 2007. Peptidylarginine deiminase (PAD) 6 is essential for oocyte cytoskeletal sheet formation and female fertility. *Mol Cell Endocrinol* **273:** 25–31. doi:10.1016/j.mce.2007.05.005

Fu B, Ma H, Liu D. 2019. Endogenous retroviruses function as gene expression regulatory elements during mammalian preimplantation embryo development. *Int J Mol Sci* **20:** 790. doi:10.3390/ijms20030790

Genet M, Torres-Padilla ME. 2020. The molecular and cellular features of 2-cell-like cells: a reference guide. *Development* **147:** dev189688. doi:10.1242/dev.189688

Geng LN, Yao Z, Snider L, Fong AP, Cech JN, Young JM, van der Maarel SM, Ruzzo WL, Gentleman RC, Tawil R, et al. 2012. DUX4 activates germline genes, retroelements, and immune mediators: implications for facioscapulohumeral dystrophy. *Dev Cell* **22:** 38–51. doi:10.1016/j.devcel.2011.11.013

Graham-Paquin AL, Saini D, Sirois J, Hossain I, Katz MS, Zhuang QK, Kwon SY, Yamanaka Y, Bourque G, Bouchard M, et al. 2023. ZMYM2 is essential for methylation of germline genes and active transposons in embryonic development. *Nucleic Acids Res* **51:** 7314–7329. doi:10.1093/nar/gkad540

Hao Y, Stuart T, Kowalski MH, Choudhary S, Hoffman P, Hartman A, Srivastava A, Molla G, Madad S, Fernandez-Granda C, et al. 2023. Dictionary learning for integrative, multimodal

and scalable single-cell analysis. *Nat Biotechnol May* **25:** 293–304. doi:10.1038/s41587-023-01767-y

Hendrickson PG, Doráis JA, Grow EJ, Whiddon JL, Lim JW, Wike CL, Weaver BD, Pflueger C, Emery BR, Wilcox AL, et al. 2017. Conserved roles of mouse DUX and human DUX4 in activating cleavage-stage genes and MERVL/HERVL retrotransposons. *Nat Genet* **49:** 925–934. doi:10.1038/ng.3844

Jachowicz JW, Bing X, Pontabry J, Bošković A, Rando OJ, Torres-Padilla ME. 2017. LINE-1 activation after fertilization regulates global chromatin accessibility in the early mouse embryo. *Nat Genet* **49:** 1502–1510. doi:10.1038/ng.3945

Jensen LJ, Kuhn M, Stark M, Chaffron S, Creevey C, Muller J, Doerks T, Julien P, Roth A, Simonovic M, et al. 2009. STRING 8--a global view on proteins and their functional interactions in 630 organisms. *Nucleic Acids Res* **37:** D412–D416. doi:10.1093/nar/gkn760

Jentoft IMA, Bäuerlein FJB, Welp LM, Cooper BH, Petrovic A, So C, Penir SM, Politi AZ, Horokhovskyi Y, Takala I, et al. 2023. Mammalian oocytes store proteins for the early embryo on cytoplasmic lattices. *Cell* **186:** 5308–5327.e25. doi:10.1016/j.cell.2023.10.003

Jiang ZY, Fan HY. 2022. Five questions toward mRNA degradation in oocytes and preimplantation embryos: when, who, to whom, how, and why? *Biol Reprod* **107:** 62–75. doi:10.1093/biolre/ioac014

Kim B, Kan R, Anguish L, Nelson LM, Coonrod SA. 2010. Potential role for MATER in cytoplasmic lattice formation in murine oocytes. *PLoS One* **5:** e12587. doi:10.1371/journal.pone.0012587

Kim D, Langmead B, Salzberg SL. 2015. HISAT: a fast spliced aligner with low memory requirements. *Nat Methods* **12:** 357–360. doi:10.1038/nmeth.3317

Kobayashi H, Sakurai T, Imai M, Takahashi N, Fukuda A, Yayoi O, Sato S, Nakabayashi K, Hata K, Sotomaru Y, et al. 2012. Contribution of intragenic DNA methylation in mouse gametic DNA methylomes to establish oocyte-specific heritable marks. *PLoS Genet* **8:** e1002440. doi:10.1371/journal.pgen.1002440

Kolberg L, Raudvere U, Kuzmin I, Vilo J, Peterson H. 2020. gprofiler2 -- an R package for gene list functional enrichment analysis and namespace conversion toolset g:Profiler. *F1000Res* **9:** 709. doi:10.12688/f1000research.24956.2

Kozak CA. 2015. Origins of the endogenous and infectious laboratory mouse γ-retroviruses. *Viruses* **7:** 1–26. doi:10.3390/v7010001

Krueger F, Andrews SR. 2011. Bismark: a flexible aligner and methylation caller for bisulfite-seq applications. *Bioinformatics* **27:** 1571–1572. doi:10.1093/bioinformatics/btr167

Li H, Durbin R. 2009. Fast and accurate short read alignment with Burrows–Wheeler transform. *Bioinformatics* **25:** 1754–1760. doi:10.1093/bioinformatics/btp324

Li L, Baibakov B, Dean J. 2008. A subcortical maternal complex essential for preimplantation mouse embryogenesis. *Dev Cell* **15:** 416–425. doi:10.1016/j.devcel.2008.07.010

Li Y, Zhang Z, Chen J, Liu W, Lai W, Liu B, Li X, Liu L, Xu S, Dong Q, et al. 2018. Stella safeguards the oocyte methylome by preventing de novo methylation mediated by DNMT1. *Nature* **564:** 136–140. doi:10.1038/s41586-018-0751-5

Love MI, Huber W, Anders S. 2014. Moderated estimation of fold change and dispersion for RNA-seq data with DESeq2. *Genome Biol* **15:** 550. doi:10.1186/s13059-014-0550-8

Macfarlan TS, Gifford WD, Driscoll S, Lettieri K, Rowe HM, Bonanomi D, Firth A, Singer O, Trono D, Pfaff SL. 2012. Embryonic stem cell potency fluctuates with endogenous retrovirus activity. *Nature* **487:** 57–63. doi:10.1038/nature11244

Maenohara S, Unoki M, Toh H, Ohishi H, Sharif J, Koseki H, Sasaki H. 2017. Role of UHRF1 in de novo DNA methylation in oocytes and maintenance methylation in preimplantation embryos. *PLoS Genet* **13:** e1007042. doi:10.1371/journal.pgen.1007042

Mahadevan S, Sathappan V, Utama B, Lorenzo I, Kaskar K, Van den Veyver IB. 2017. Maternally expressed NLRP2 links the subcortical maternal complex (SCMC) to fertility, embryogenesis and epigenetic reprogramming. *Sci Rep* **7:** 44667. doi:10.1038/srep44667

Meng TG, Guo JN, Zhu L, Yin Y, Wang F, Han ZM, Lei L, Ma XS, Xue Y, Yue W, et al. 2023. NLRP14 safeguards calcium homeostasis via regulating the K27 ubiquitination of Nclx in oocyte-to-embryo transition. *Adv Sci (Weinh)* **10:** e2301940. doi:10.1002/advs.202301940

Monk D, Mackay DJG, Eggermann T, Maher ER, Riccio A. 2019. Genomic imprinting disorders: lessons on how genome, epigenome and environment interact. *Nat Rev Genet* **20:** 235–248. doi:10.1038/s41576-018-0092-0

Moor RM, Osborn JC, Crosby IM. 1985. Gonadotrophin-induced abnormalities in sheep oocytes after superovulation. *J Reprod Fertil* **74:** 167–172. doi:10.1530/jrf.0.0740167

Pettersen EF, Goddard TD, Huang CC, Couch GS, Greenblatt DM, Meng EC, Ferrin TE. 2004. UCSF chimera—a visualization system for exploratory research and analysis. *J Comput Chem* **25:** 1605–1612. doi:10.1002/jcc.20084

Pires DE, Ascher DB, Blundell TL. 2014a. DUET: a server for predicting effects of mutations on protein stability using an integrated computational approach. *Nucleic Acids Res* **42:** W314–W319. doi:10.1093/nar/gku411

Pires DE, Ascher DB, Blundell TL. 2014b. mCSM: predicting the effects of mutations in proteins using graph-based signatures. *Bioinformatics* **30:** 335–342. doi:10.1093/bioinformatics/btt691

Qian J, Nguyen NMP, Rezaei M, Huang B, Tao Y, Zhang X, Cheng Q, Yang H, Asangla A, Majewski J, et al. 2018. Biallelic PADI6 variants linking infertility, miscarriages, and hydatidiform moles. *Eur J Hum Genet* **26:** 1007–1013. doi:10.1038/s41431-018-0141-3

Raijmakers R, Zendman AJ, Egberts WV, Vossenaar ER, Raats J, Soede-Huijbregts C, Rutjes FP, van Veelen PA, Drijfhout JW, Pruijn GJ. 2007. Methylation of arginine residues interferes with citrullination by peptidylarginine deiminases in vitro. *J Mol Biol* **367:** 1118–1129. doi:10.1016/j.jmb.2007.01.054

Rausch T, Zichner T, Schlattl A, Stütz AM, Benes V, Korbel JO. 2012. DELLY: structural variant discovery by integrated paired-end and split-read analysis. *Bioinformatics* **28:** i333–i339. doi:10.1093/bioinformatics/bts378

Rodrigues CH, Pires DE, Ascher DB. 2018. DynaMut: predicting the impact of mutations on protein conformation, flexibility and stability. *Nucleic Acids Res* **46:** W350–W355. doi:10.1093/nar/gky300

Rong Y, Ji SY, Zhu YZ, Wu YW, Shen L, Fan HY. 2019. ZAR1 and ZAR2 are required for oocyte meiotic maturation by regulating the maternal transcriptome and mRNA translational activation. *Nucleic Acids Res* **47:** 11387–11402. doi:10.1093/nar/gkz863

Sakashita A, Kitano T, Ishizu H, Guo Y, Masuda H, Ariura M, Murano K, Siomi H. 2023. Transcription of MERVL retrotransposons is required for preimplantation embryo development. *Nat Genet* **55:** 484–495. doi:10.1038/s41588-023-01324-y

Sendžikaitė G, Kelsey G. 2019. The role and mechanisms of DNA methylation in the oocyte. *Essays Biochem* **63:** 691–705. doi:10.1042/EBC20190043

Smallwood SA, Tomizawa S, Krueger F, Ruf N, Carli N, Segonds-Pichon A, Sato S, Hata K, Andrews SR, Kelsey G. 2011. Dynamic CpG island methylation landscape in oocytes and preimplantation embryos. *Nat Genet* **43:** 811–814. doi:10.1038/ng.864

Sookdeo A, Hepp CM, McClure MA, Boissinot S. 2013. Revisiting the evolution of mouse LINE-1 in the genomic era. *Mob DNA* **4:** 3. doi:10.1186/1759-8753-4-3

Sugie K, Funaya S, Kawamura M, Nakamura T, Suzuki MG, Aoki F. 2020. Expression of Dux family genes in early preimplantation embryos. *Sci Rep* **10:** 19396. doi:10.1038/s41598-020-76538-9

Taft R. 2017. In vitro fertilization in mice. *Cold Spring Harb Protoc* **2017:** pdb.prot094508. doi:10.1101/pdb.prot094508

Valley CC, Cembran A, Perlmutter JD, Lewis AK, Labello NP, Gao J, Sachs JN. 2012. The methionine–aromatic motif plays a unique role in stabilizing protein structure. *J Biol Chem* **287:** 34979–34991. doi:10.1074/jbc.M112.374504

Varadi M, Anyango S, Deshpande M, Nair S, Natassia C, Yordanova G, Yuan D, Stroe O, Wood G, Laydon A, et al. 2022. AlphaFold protein structure database: massively expanding the structural coverage of protein-sequence space with high-accuracy models. *Nucleic Acids Res* **50:** D439–D444. doi:10.1093/nar/gkab1061

Veselovska L, Smallwood SA, Saadeh H, Stewart KR, Krueger F, Maupetit-Méhouas S, Arnaud P, Tomizawa S, Andrews S, Kelsey G. 2015. Deep sequencing and de novo assembly of the mouse oocyte transcriptome define the contribution of transcription to the DNA methylation landscape. *Genome Biol* **16:** 209. doi:10.1186/s13059-015-0769-z

Wang M, Chen Z, Zhang Y. 2022. CBP/p300 and HDAC activities regulate H3K27 acetylation dynamics and zygotic genome activation in mouse preimplantation embryos. *EMBO J* **41:** e112012. doi:10.15252/embj.2022112012

Williams JPC, Walport LJ. 2023. PADI6: what we know about the elusive fifth member of the peptidyl arginine deiminase family. *Philos Trans R Soc Lond B Biol Sci* **378:** 20220242. doi:10.1098/rstb.2022.0242

Yan R, Cheng X, Gu C, Xu Y, Long X, Zhai J, Sun F, Qian J, Du Y, Wang H, et al. 2023. Dynamics of DNA hydroxymethylation and methylation during mouse embryonic and germline development. *Nat Genet* **55:** 130–143. doi:10.1038/s41588-022-01258-x

Yurttas P, Vitale AM, Fitzhenry RJ, Cohen-Gould L, Wu W, Gossen JA, Coonrod SA. 2008. Role for PADI6 and the cytoplasmic lattices in ribosomal storage in oocytes and translational control in the early mouse embryo. *Development* **135:** 2627–2636. doi:10.1242/dev.016329

Zhao ZH, Ma JY, Meng TG, Wang ZB, Yue W, Zhou Q, Li S, Feng X, Hou Y, Schatten H, et al. 2020. Single-cell RNA sequencing reveals the landscape of early female germ cell development. *FASEB J* **34:** 12634–12645. doi:10.1096/fj.202001034RR

Zheng W, Zhou Z, Sha Q, Niu X, Sun X, Shi J, Zhao L, Zhang S, Dai J, Cai S, et al. 2020. Homozygous mutations in BTG4 cause zygotic cleavage failure and female infertility. *Am J Hum Genet* **107:** 24–33. doi:10.1016/j.ajhg.2020.05.010

A maternal-effect *Padi6* variant causes nuclear and cytoplasmic abnormalities in oocytes, as well as failure of epigenetic reprogramming and zygotic genome activation in embryos

Carlo Giaccari, Francesco Cecere, Lucia Argenziano, et al.

Genes Dev. published online March 7, 2024
Access the most recent version at doi:10.1101/gad.351238.123